Published in final edited form as:

Nat Aging. 2023 February ; 3(2): 173–184. doi:10.1038/s43587-022-00354-1.

Impaired dynamics of precapillary sphincters and pericytes at first-order capillaries predict reduced neurovascular function in the aging mouse brain

Changsi Cai[1,7,✉], **Stefan Andreas Zambach**[1,7], **Søren Grubb**[1], **Lechan Tao**[1,2], **Chen He**[1], **Barbara Lykke Lind**[1], **Kirsten Joan Thomsen**[1], **Xiao Zhang**[1], **Bjørn Olav Hald**[1], **Reena Murmu Nielsen**[1], **Kayeon Kim**[1], **Anna Devor**[3,4], **Micael Lønstrup**[1], **Martin Johannes Lauritzen**[1,5,6,✉]

[1]Department of Neuroscience, Faculty of Health and Medical Science, University of Copenhagen, Copenhagen, Denmark.

[2]School of Biomedical Engineering, Shanghai Jiao-Tong University, Shanghai, China.

[3]Department of Biomedical Engineering, Boston University, Boston, MA, USA.

[4]Athinoula A. Martinos Center for Biomedical Imaging, Department of Radiology, Harvard Medical School, Massachusetts General Hospital, Charlestown, MA, USA.

[5]Department of Clinical Neurophysiology, Rigshospitalet, Copenhagen, Denmark.

[6]Center for Healthy Aging, Faculty of Health and Medical Science, University of Copenhagen, Copenhagen, Denmark.

[7]These authors contributed equally: Changsi Cai, Stefan Andreas Zambach.

Abstract

The microvascular inflow tract, comprising the penetrating arterioles, precapillary sphincters and first-order capillaries, is the bottleneck for brain blood flow and energy supply. Exactly how aging alters the structure and function of the microvascular inflow tract remains unclear. By in vivo four-dimensional two-photon imaging, we reveal an age-dependent decrease in vaso-

---

✉**Correspondence and requests for materials** should be addressed to Changsi Cai or Martin Johannes Lauritzen. ccai@sund.ku.dk; mlauritz@sund.ku.dk.

Author contributions

C.C., S.A.Z. and M.J.L. designed research; S.A.Z., C.C., S.G., L.T., C.H., K.J.T., X.Z., B.O.H., R.M.N. and M.L. performed research; C.C. and K.K. contributed new reagents/analytic tools; S.A.Z., C.C., S.G. and B.K.L. analyzed data; S.A.Z., C.C., A.D. and M.J.L. wrote the paper.

Competing interests

The authors declare no competing interests.

Reporting summary

Further information on research design is available in the Nature Portfolio Reporting Summary linked to this article.

Extended data is available for this paper at https://doi.org/10.1038/s43587-022-00354-1.

Supplementary information The online version contains supplementary material available at https://doi.org/10.1038/s43587-022-00354-1.

Peer review information *Nature Aging* thanks Stephanie Bonney, Yongsoo Kim and Anusha Mishra for their contribution to the peer review of this work.

responsivity accompanied by a decrease in vessel density close to the arterioles and loss of vascular mural cell processes, although the number of mural cell somas and their alpha smooth muscle actin density were preserved. The age-related reduction in vascular reactivity was mostly pronounced at precapillary sphincters, highlighting their crucial role in capillary blood flow regulation. Mathematical modeling revealed impaired pressure and flow control in aged mice during vasoconstriction. Interventions that preserve dynamics of cerebral blood vessels may ameliorate age-related decreases in blood flow and prevent brain frailty.

In the aging brain, the global level of cerebral blood flow (CBF) is reduced, although the energy consumption is relatively preserved[1,2]. In addition, neurovascular coupling (NVC), that is, the increase in CBF that accompanies increased brain activity, is impaired, whereas the activity-dependent increases in oxygen consumption are preserved or increased[3,4]. The alterations in cerebrovascular function challenge how well the aged brain can cope with brain diseases[5,6]. Recent data suggest that brain pericytes fail to control key neurovascular functions in aged mice and that neurovascular dysfunction precedes age-related impairments in cognitive decline[7]. However, the exact vascular mechanisms are not well understood. In this study, we focused on the contribution of functional compartments of the microvascular inflow tract (MIT), which comprises arterioles, precapillary sphincters and arteriolar capillaries[8]. The MIT is thought to play a key role in NVC[9]. In particular, precapillary sphincters at the junction of the penetrating arteriole (PA) and its initial branch (first-order capillary) are crucial in maintaining capillary perfusion and are bottlenecks for brain energy supply[10,11]. We provide evidence that impaired NVC in the aging brain is linked to alterations in vascular reactivity and mural cell coverage at specific zones of the MIT.

Results

Neurovascular coupling at the microvascular inflow tract is reduced with age

We used NG2-DsRed mice expressing red fluorescent protein in vascular mural cells (pericytes and vascular smooth muscle cells) under the NG2 promoter. Adult mice that were 3–12 months of age and old mice that were 20–28 months of age were examined in the experiments. Fluorescein isothiocyanate (FITC)-dextran was injected intravenously to stain vessel lumens (Fig. 1a,b). Using in vivo two-photon microscopy, we classified capillaries by their branching orders, with the first order being the first capillary branching from the PA, and so forth (Fig. 1b). We did not classify the morphology of vascular mural cells, as DsRed reporters may not be bright enough to examine the morphology of fine processes of mural cells.

We used fast and repetitive four-dimensional (4D) two-photon microscopy to examine NVC of the MIT in the somatosensory cortex of anesthetized mice, minimizing the effect of focus drift on vessel diameter measurement. Precapillary sphincters were identified as the indentation between the PA and the first-order capillary with thick mural cells enwrapping the lumen (Fig. 1b)[11]. We used whisker-pad (WP) electrical stimulation for NVC studies. WP electrical stimulation with 1.5 mA at 2 Hz for 20 s induced vasodilation, followed by a small undershoot at the PA, precapillary sphincter and the first-order capillary (Fig. 1c–f). Dilation amplitude (relative change in diameter), absolute increases in diameter and cross-sectional area change (based on diameters) declined with age (Fig. 1g and Extended Data Fig. 1a,b). We also noted an age-associated decrease in the extent of the undershoot at PAs and pre-capillary sphincters (Fig. 1h). To compare the response time in adult and old mice, we defined onset of dilation as the time point at half of the peak amplitude and dilation duration as half-peak width. The onset of dilation did not differ between adult and aged mice (Fig. 1i), but the dilation duration was shorter at all vascular locations in old mice (Fig. 1j). Peak diameters at PAs and sphincters decreased with age (Extended Data Fig. 1c), suggesting higher vessel stiffness in old mice.

To examine whether the reduced vascular responsivity was associated with decreased neural activity in the aged brain, we inserted a glass micropipette to record local field potentials (LFPs; Fig. 1k). WP stimulation-induced field excitatory postsynaptic potentials (fEPSPs). The amplitude, latency and area under the curve of the fEPSPs were preserved with age (Fig. 1l–n), indicating that excitatory synaptic responses were unchanged by aging.

Overall, the mismatch between preserved LFPs and the reduction in the NVC response in aged mice suggests a decrease in vascular responsivity to rises in excitatory neurotransmission, the main driving force for NVC[1,12].

Reduced neurovascular coupling in the aging brain is dependent on microvascular mural cells

The next question we addressed was whether the decrease in NVC responses with age represented a general decrease in vascular responsivity. To selectively activate vascular mural cells, we locally puffed pinacidil, an ATP-sensitive potassium channel (K_{ATP} channel) opener, via a glass micropipette in proximity to the imaged vessels. Our previous work suggested that 5 mM pinacidil acts directly on vascular mural cells without eliciting neuronal or astrocytic responses[11]. Pinacidil at 5 mM evoked vasodilation at all MIT locations: the PA, precapillary sphincter and first-order to third-order capillaries (Fig. 1o–s). Compared with adult brains, PAs, precapillary sphincters and first-order capillaries exhibited smaller dilation amplitudes, absolute diameter changes and cross-sectional area changes with age, whereas the responsivity was the same for second-order and third-order capillaries (Fig. 1s and Extended Data Fig. 1d,e). Note that the initial diameter drop was due to a momentary mechanical pressure change caused by puffing (Extended Data Fig. 2).

The reduced vasodilator responses in aged brains may be explained, in part, by vessel stiffness due to a reduction in the number of elastin fibers and the fragmentation of elastin, along with the deposition of collagens[13,14]. To test this hypothesis, we puffed 10 mM papaverine on MIT in adult and aged mice. Papaverine dilates blood vessels by inhibiting voltage-gated calcium channels[15] and by blocking vascular phosphodiesterases[16], preventing degradation of cGMP and cAMP[17]. After application of papaverine, the remaining elements to constrain dilation may be passive structures, such as elastin and collagen[10,18]. Papaverine elicited vasodilation in adult mice, but its effect in aged mice was attenuated (Fig. 2a–c and Extended Data Fig. 1g,h). In particular, the response to papaverine was reduced at precapillary sphincters, providing evidence of age-related changes specifically at this vascular zone, likely attributable to vessel stiffness.

The vasodilation induced by local papaverine application was smaller than that induced by WP stimulation and pinacidil puffing in aged mice, but these vasodilator responses were similar in adult mice (Extended Data Fig. 3). Endothelial nitric oxide synthase (eNOS) activity has been reported to decline with age[19], partially due to an increase in the endogenous inhibitor of eNOS[20]. To investigate whether ongoing nitric oxide (NO) synthesis is altered at the MIT with age, we intravenously infused the NOS inhibitor NG-nitro-L-arginine methyl ester (L-NAME) at a dose of 30 mg per kg body weight. L-NAME induced vasoconstriction at the PA, precapillary sphincter, and first-order to third-order capillaries in adult mice, but to a lesser extent in aged mice (Fig. 2d–g). PAs constricted less at the 2nd, 3rd and 4th minutes and precapillary sphincters constricted less at the 3rd and 4th minute after L-NAME infusion in aged mice (Fig. 2i), as reflected in the constriction amplitude in percentage, absolute diameter and cross-sectional area change (Fig. 2h and Extended Data Fig. 1j,k). This indicates NO synthesis or NO-dependent mechanisms are impaired with age. Taken together, the results indicate that age affects the MIT by impairing vasodilator sensitivity in the whole MIT and affecting responsivity, particularly at precapillary sphincters.

Vasoconstriction at precapillary sphincters decreases with age

Having established that the responsivity of vascular mural cells at MIT decreases with age, with less pronounced vasoconstriction by L-NAME infusion in aged mice, we examined whether aging affects vasoconstriction at MIT. For this purpose, we used endothelin (ET1), a potent vasoconstrictor that is synthesized mainly by endothelial cells in brain pathology[21]. Local puffing of 0.5 μM ET1 using glass micropipettes elicited strong and long-lasting vasoconstriction at all examined MIT locations in both adult and old mice (Fig. 2j–m). The contractility of mural cells was largely preserved with age, except at precapillary sphincters, which presented reduced responsivity (Fig. 2n and Extended Data Fig. 1m,n).

Therefore, with age, the PA and first-order to third-order capillaries preserve their ability to constrict, and precapillary sphincters are less contractile. This indicates that the vascular network in healthy old mice may successfully maintain a rate of flow that mitigates exogenous vasoconstriction and prevents an energy crisis, particularly via precapillary sphincters.

Vascular coverage of mural cell processes decreases with age

Capillary pericyte loss during aging has been reported[22], although a recent transcriptomic study shows no change[23]. More detailed knowledge of MIT mural cells in old mice is lacking. To further characterize aging-associated morphological changes in vascular mural cells, we used immunohistochemistry to stain alpha smooth muscle actin (αSMA) in vascular mural cells of the MIT (Fig. 3a,b and Extended Data Fig. 4). The brains were prepared in the same batch to minimize variability and to ensure the comparability of antibody staining in all brain slices. For image analysis, we normalized the background of each x–y plane in one acquired image z-stack to minimize differences in crossplane fluorescence intensity (Methods and Extended Data Fig. 5a,b).

We examined whether aging caused an alteration in mural cell αSMA or morphology. Similarly to previous studies, the density of nuclei in non-vascular brain cells decreased dramatically with age (Extended Data Fig. 5c). In this study, we discovered that mural cell coverage of the vessel surface area declined at PAs and at first-order to third-order capillaries but was preserved at the precapillary sphincters (Fig. 3c). On the other hand, the linear density of mural cell somas, that is, the number of mural cell somas per millimeter of vessel length, remained constant with age (Fig. 3d). Similarly, the vascular density of endothelial cell somas and ratio of mural cell somas to endothelial cell somas were preserved with age (Extended Data Fig. 5d and Fig. 3e). We also measured the αSMA density at mural cells (that is, the NG2-positive area). αSMA density was unaltered with age (Fig. 3f), suggesting that brain vascular aging is unrelated to mural cell loss or αSMA degeneration at the MIT, but accompanied by lower vascular mural cell process coverage by mural cell processes on PAs and first-order to third-order capillaries.

Vessel density declines and diameter increases with age

To further characterize the morphological and structural changes of the MIT, we recorded two-photon image stacks of PAs and their associated capillary networks in adult and aged mice in vivo (Fig. 4a). Image stacks were skeletonized to estimate vessel length and diameter by Amira software (Methods and Fig. 4b,c). We manually labeled individual PAs and first-order to fifth-order capillaries by visual inspection. Similarly to recent studies[24], we used total length per brain volume as a measurement of vessel density (Fig. 4d–f). The total length of the PAs and first-order to fourth-order capillaries declined with age, whereas the total length of ≥ fifth-order capillaries was preserved (Fig. 4e). This implies that the vessel density declines with age in proximity to the PA, but not in the capillary bed on the venous side. We also used total vessel number and mean vessel length to estimate the vessel density and rarefaction of vascular networks. We found that the total vessel number decreased with age, especially in proximity to the PA (Extended Data Fig. 6a–c), while mean vessel length increased with age at PA and in proximity to the venous side (Extended Data Fig. 6d–f). Finally, we asked whether this dependency changed with depth. Our data show that the age-related decline in vessel density occurred at all cortical layers (Fig. 4f and Extended Data Fig. 6c).

Consistent with previous reports[2], vessel diameters increased with age for all examined vessel locations (Fig. 4g,h), but were only significant at a depth of 0–200 μm (Fig. 4i). Considering that the mean vessel diameter increased and total vessel length decreased with age, we examined the total vessel volume (Extended Data Fig. 6g–i) as a proxy for brain perfusion capacity. Interestingly, the global vessel volume increased with age (Extended Data Fig. 6g) as result of an increase in the volume of the venous capillaries (Extended Data Fig. 6h), which may suggest that brain vascular aging is associated with an increase in venous compliance. Lastly, we estimated vessel tortuosity in both adult and old brains by dividing the curved length by the chord length of each vessel segment (tortuosity index; Fig. 4j–l). The PAs became more tortuous with age, whereas vessels downstream from the PA remained at the same level of tortuosity (Fig. 4k,l).

Taken together, the results suggest that the vessel density decreases close to the PA; vessel total volume increases close to ascending venules; the vessel changes are similar for cortical layers I-III; and vessel tortuosity increases at the PA, but not in capillaries.

Blood flow and pressure at the microvascular inflow tract are affected by aging

To assess the possible implications of a special role for the sphincter and first-order capillary on capillary flow and pressure, we developed a mathematical model based on three-dimensional reconstruction of brain vasculatures from three adult mice and three old mice, including all elements of the MIT and up to the sixth-order capillary (Extended Data Fig. 7a,b,e). The model assumed that the vessels were rigid and the flow laminar. We calculated the flow resistance at each capillary order using Poiseuille's law. Given that the sum of flows entering and leaving any internal node equals zero (Kirchoff's 2nd law), we calculated the blood pressure and flow at each node within the vascular network using Ohm's law. We designated vessel diameters and dilation and constriction amplitudes based on two-photon microscopy imaging (Supplementary Table 1).

We calculated the pressure distribution in the adult and aged vascular network models at the resting state, during WP stimulation and during ET1 puffing (Extended Data Fig. 7c). Our model suggested that, in old mice, first-order to third-order capillaries (but not the PAs or precapillary sphincters) were exposed to higher intraluminal pressure than in adult mice, particularly when exposed to ET1 (Extended Data Fig. 7c). To examine whether pressures at all three states (rest, WP and ET1) were related to the degree of mural cell coverage reported in Fig. 3, we plotted mural cell coverage as a function of blood pressure for adult and old mice (Extended Data Fig. 7d). The analysis suggests that the blood pressure distribution correlates with mural cell coverage in an almost linear manner from sphincters to the third-order capillaries. With age, mural cell coverage decreased, whereas pressure increased at the first-order to third-order capillaries, suggesting a more fragile regulation of blood pressure at MIT in aged mice.

Next, we compared the blood flow distribution in adult and old mice at each vessel location (Extended Data Fig. 7e,f). Given that the mean vessel diameter was larger in the aged brain than in the adult brain, the flow at PAs was higher in old mice than in adult mice at rest (Extended Data Fig. 7f). Although the age-related flow difference was insignificant for WP stimulation, the flow drop was reduced at precapillary sphincters and first-order to third-order capillaries in old brains after ET1 puffing (Extended Data Fig. 7f).

Discussion

Using in vivo 4D two-photon microscopy, immunohistochemistry and mathematical modeling, we examined the structural and functional changes that occur in brain microvasculature with age. We focused on the MIT: the PAs, precapillary sphincters and first few orders of capillaries, which play important roles in regulating capillary blood flow. Our study shows that, at the MIT, vascular responsivity decreased with age, contributing to the reduction in NVC responses in aged mice. In addition, the decrease in vascular dilation may be ascribed to an impaired ability of vascular mural cells, especially precapillary sphincters, to relax. In comparison, the ability of vessels to constrict in response to ET1 was preserved with age, except for precapillary sphincters, which constricted less in old than in adult mice. Coverage of MIT by mural cell processes was reduced with age, but mural cell soma and αSMA densities remained unaltered. Capillary density decreased in proximity to the PA, but vessel diameters increased at all locations, reducing the overall vascular resistance. Mathematical modeling suggested impaired regulation of blood pressure at MIT but implied preserved blood flow at MIT during vasoconstriction.

Studies have found that vascular tone in middle-aged mice and rats may be increased[25], or decreased[26]. Here we used mice that were more than 90 weeks old, and this revealed an increase in the resting vessel diameter that may reflect a decrease in vascular tone produced by age-related changes in autoregulation[27]. Our findings of increased resting-state vessel diameter could reflect a mechanism that old brains use to cope with reduced vasomotility by increasing resting-state flow. ET1-evoked vasoconstriction at sphincters was smaller in old than in adult mice, suggesting that the aged vascular network aims to maintain a rate of blood flow that preserves the brain’s energy supply. Further, the total vessel length was decreased but resting diameter increased with age, a constant blood volume was maintained. Our findings could suggest a compensating mechanism to keep CBF and oxygen supply at a physiologically healthy level during brain aging. It cannot be excluded that the aged vascular system is strained by the reduced vascular capacity for dilation and that energy crisis may therefore be more likely to occur under homeostatic stress.

K_{ATP} channels are generally downregulated during aging[28] and there is an age-related decrease in the probability of K_{ATP} channels opening[29]. NO production and bioavailability is reduced during aging[30], but the mechanism is still unclear, since eNOS has been reported not to change[31], increase[32] or decrease[33] with age. This discrepancy may be attributed to differences among mouse strains, specimens and preparations. ET1 signaling and synthesis are increased in old compared with adult brains[34], and ETA receptor expression in rat heart is reported to decrease with age[35], but it is not known if this is true for brain microvessels. If the same reduction in ETA occurs in brain aging, our results showing that aged precapillary sphincters constricted less than adult may be caused by the loss of receptors and consequent desensitization. Our studies of NO and ET1 in aged mice suggest that the response of vascular mural cells to signaling molecules produced by endothelial cells is either preserved or reduced with age. This is consistent with the canonical view that impaired interplay between endothelial cells and mural cells is the hallmark of vascular damage in advanced aging[36] (Extended Data Fig. 8).

Immunohistochemistry of vascular mural cell morphology and αSMA density showed preservation of αSMA density in mural cells with age, whereas mural cell coverage by their processes decreased at the MIT, probably due to diminished pericyte outgrowth from aged pericytes compared with that of their younger counterparts. Preservation of mural cell soma density suggests that aging leads to a reduction in mural cell complexity. This is similar to neuron number preservation with reduced dendrite lengths and numbers during normal aging[37]. Pericyte process rarefaction could contribute to the dysregulation of blood flow at the MIT and may impact the blood–brain barrier[38], and loss of pericyte function is associated with blood flow reduction in neurodegeneration[39]. The age-related alteration of blood flow regulation was most pronounced at precapillary sphincters, which are encircled by a bulky mural cell, but mural cells at sphincters do not have long fine processes and the reduction in responsivity at this site is not explained by the decrease in vessel coverage by mural cell processes. Alternatively, future studies should quantify the extracellular matrix during aging, with particular focus on the sphincters.

In summary, our data reveal important roles for the precapillary sphincters and first-order capillaries in healthy brain aging, and imply the existence of age-related effects that compensate for vasoconstriction to help maintain tissue perfusion.

Methods

Animal handling

All procedures were approved by the Danish National Ethics Committee according to the guidelines set forth in the European Council's Convention for the Protection of Vertebrate Animals used for Experimental and Other Scientific Purposes and are in compliance with the ARRIVE guidelines. A total of 63 NG2-DsRed mice Tg (cspg4-DsRed. T1)1Akik/j from Jackson laboratory, including 32 adult mice (aged 3–12 months) and 31 old mice (aged 20–28 months), were used. All mice were maintained at 21 °C ± 1 °C with 50% ± 10% relative humidity, and a 12-h light/12-h dark cycle (06:00–18:00). Food and water were provided ad libitum. The mouse trachea was cannulated for mechanical ventilation. One catheter was inserted into the left femoral artery to monitor blood pressure and blood gases; a second catheter was placed into the left femoral vein for infusion of substances. To maintain the mouse under physiological conditions, we continuously monitored end-expiratory CO_2, blood pressure, heart rate and O_2 saturation at the right hind paw. Throughout the experiment, we assessed blood gases in arterial blood samples twice (55 µl each time): after completion of the craniotomy and after termination of the experiments just before euthanasia. We monitored the mouse's physiological state at pO_2 95–110 mm Hg, pCO_2 30–40 mm Hg and pH 7.35–7.45. Body temperature was maintained at 37 °C using a rectal temperature probe and heating blanket. We drilled a 4-mm-diameter craniotomy above the sensory barrel cortex region, centered 0.5 mm behind and 3 mm to the right of bregma. After dura removal, the preparation was covered with 0.75% agarose gel, further submerged under artificial cerebrospinal fluid (aCSF; 120 mM NaCl, 2.8 mM KCl, 22 mM $NaHCO_3$, 1.45 mM $CaCl_2$, 1 mM Na_2HPO_4, 0.876 mM $MgCl_2$ and glucose 2.55 mM; pH 7.4), and kept at 37 °C. For imaging experiments, three-quarters of the craniotomy was covered with a tilted glass coverslip that permitted the insertion of glass micropipettes. The mice were anesthetized by intraperitoneal injection of xylazine (10 mg per kg body weight) followed by ketamine (60 mg per kg body weight), and maintained during surgery with supplemental doses (30 mg per kg body weight) of ketamine every 24 min. Upon completion of all surgical procedures, the anesthesia was switched to continuous intravenous infusion with a mixture of 17% α-chloralose and 2% FITC-dextran (0.02 ml per 10 g body weight per hour). At the end of the experimental protocol, the mice were euthanized by intravenous injection of 0.05 ml pentobarbital followed by cervical dislocation.

Whisker-pad stimulation

The mouse sensory barrel cortex was activated by stimulating the contralateral ramus infraorbitalis (IO) of the trigeminal nerve via a set of custom-made bipolar electrodes inserted percutaneously. The cathode was positioned according to the hiatus IO, and the anode was inserted into the masticatory muscles. WP stimulation (thalamocortical IO stimulation) was performed at an intensity of 1.5 mA with pulse duration of 1 ms, duration of 20 s and frequency of 2 Hz.

Local ejection (puffing) by glass micropipette

We used a pipette puller (P-97, Sutter Instrument) to produce borosilicate glass micropipettes with a resistance of 3–3.5 MΩ. The pipette was loaded with a mixture of 10 μM Alexa 594 and vasoactive substances of interest, which enabled visualization of the pipette tip under an epifluorescence camera and two-photon microscope. Guided first by epifluorescence imaging, and then by two-photon microscopy, the pipette was carefully inserted into the cortex and moved in proximity of the targeted vessels. The distance between the pipette tip and the vasculature was approximately 30–50 μm. Pressure ejection of vasoactive substances was achieved using an air pressure pump at 8–15 psi. A red cloud (Alexa 594) ejected from the pipette tip was visually observed to cover the local vascular region instantaneously, and the background returned to normal approximately 1 min after puffing. An estimated volume of 0.38 nl was delivered in each puff. This high concentration is rapidly diluted. The drug concentration in the puffing solution was higher than the concentration of the same drug used in brain surface superfusion experiments. An electrode inside the puffing pipette was used to record local electrical brain activity during the experiments. This ensured that LFPs were recorded at the location where the concentration of the puffed drug was the highest.

Local field potentials

To record extracellular LFPs, we used the same glass micropipette for the puffing experiments. The Ag/AgCl ground electrode was positioned in the neck muscles. The signal was initially amplified using a differential amplifier (10× gain, 0.1–10,000 Hz bandwidth; DP311, Warner Instruments). Then additional amplification was performed using the CyberAmp 380 (100× gain, 0.1–10,000 Hz bandwidth; Axon Instruments). The electrical signal was digitally sampled at a 5-kHz sampling rate using the MICRO 1401 interface (Cambridge Electronic Design) connected to Spike2 software v7.02a (Cambridge Electronic Design). For each stimulation train, we averaged the LFPs, and calculated the amplitudes of fEPSPs as the difference between baseline and the first negative peak, and the latency as the time from stimulation onset to the peak of the fEPSP.

Two-photon imaging

FITC-dextran (500,000 MW, 50 μl, Sigma-Aldrich) was applied intravenously to stain the vessel lumen green. Before two-photon imaging, 4% wt/vol FITC-dextran was administered as a bolus into the femoral vein. During two-photon imaging, 2% FITC-dextran was continuously infused at a slow speed to compensate for the metabolic loss of FITC-dextran. Fast repetitive hyperstack imaging (4D imaging) was performed using a commercial two-photon microscope (Femto3D-RC microscope and Femtonics MES v6 software, Femtonics) and a ×25 1.0-NA piezo motor objective. This method compensates for focus drift and allows for evaluation of the vasculature spanning a certain *z*-axis range. Each image stack was acquired within 1 s and comprised 10–14 planes with a plane distance of 4–5 μm. This approach covered the whole *z*-axis range of the investigated blood vessels. The pixel sizes in the *x*–*y* plane were 0.2–0.38 μm. The excitation wavelength was set to 900 nm. The emitted light was filtered to collect red and green light from DsRed (smooth muscle cells and pericytes) and FITC-dextran (vessel lumens), respectively.

Two-photon imaging data analysis

The imaging analytical tool was custom made using MATLAB R2018a. To measure vessel diameter in the hyperstack video, we flattened each image stack onto one image by maximal intensity projection, creating a two-dimensional time-lapse movie. An averaged image over time from the green channel was plotted for placement of regions of interest (ROIs). Rectangular ROIs with a width of 4 μm were drawn perpendicular across the vessel longitude. The rectangular ROI was averaged by projection into one line for each frame, representing the profile of the vessel segment at this frame. The profile line was plotted as a two-dimensional image with the *x* axis as the number of frames. Chan-Vese segmentation or pixel intensity-based segmentation was used to delineate the vessel edge and estimate the diameter change in the vessel segment at this ROI. Less than 2% of the evoked diameter change was considered non-responding but included in the analysis as zero values. Up to five ROIs with an adjacent distance of 10 μm were placed at the same order capillary depending on the length of the capillary order. Diameter curves at the same order capillary were averaged, representing the response curve at this capillary order. The relative response amplitude was defined as the largest vasodilation/constriction amplitude (as a percentage) after WP stimulation/puffing. The response latency was defined as the latency of the half-maximum amplitude. The response duration was defined as the period between half-peaks of rising and falling phases. The cross-sectional area of a vessel was calculated as the square of the radius multiplied by the math constant pi, assuming that the cross-section of a vessel is a circle.

Three-dimensional vascular reconstruction and analysis by Amira

In a dedicated set of in vivo experiments, we recorded *z*-stacks in a 250–500 μm × 250–500 μm area in steps of 1–2 μm around as many PAs in the craniotomy as possible and as deep as 600 μm below the pial surface. For this purpose, we used FITC-dextran-injected adult or aged NG2-DsRed or C57BL/6 mice. The laser wavelength was set to 920 nm, and the laser power was gradually increased with imaging depth until the signal/noise ratio was too high to resolve the vessels. We did not observe any indications of laser damage, or even bleaching of the NG2-DsRed caused by the *z*-stack recordings. The angioarchitecture was analyzed by skeletonization in Amira version 6.1 (Thermo Fisher) after applying a Gaussian filter and local thresholding. We manually cleaned the skeleton from runts (small terminal branches that were obvious mistakes) and labeled the arteries and venules before incrementally labeling the first-order to fifth-order capillaries. The capillaries were always labeled the lowest order possible. The data were exported from Amira and analyzed in MATLAB using a custom-made algorithm.

Drug application

We locally ejected vasoactive substances (pinacidil, papaverine, endothelin) via a glass micropipette. Pinacidil monohydrate (P154, Sigma-Aldrich) and papaverine (P3510, Sigma-Aldrich) were solubilized in dimethylsulfoxide and further dissolved with aCSF. ET1 (1160, Tocris) was directly dissolved in aCSF. Aliquots were stored at −20 °C. L-NAME (N5751, Sigma-Aldrich) was dissolved in saline and stored at −20 °C. L-NAME was intravenously injected as a bolus at a dose of 30 mg per kg body weight. Before each experiment, each drug solution used for puffing was mixed at a 1:1 ratio with 20 μM Alexa 594 (dissolved in aCSF). Concentrations in the final puffing solution were as follows: 5 mM pinacidil, 10 mM papaverine and 0.0005 mM ET1.

Immunohistochemistry

Three adult and three old NG2-DsRed mice were transcardially perfused with 4% paraformaldehyde and their brains extracted and stored in paraformaldehyde for 4 h. The brains were then cryoprotected in PBS with 30% sucrose and 0.1% sodium azide for 48 h, rapidly frozen on dry ice-chilled isopentane, trimmed to only include the somatosensory cortex, and sectioned into coronal 50-μm-thick slices using a cryostat. Sections were rinsed in 0.1 M PBS for 5 min three times. The sections were permeabilized and blocked in 0.5% Triton-X 100 in 1× PBS (pH 7.2) and 1% bovine serum albumin overnight at 4 °C. The sections were further incubated for two nights at 4 °C with mouse ACTA2-FITC antibody (1:200 dilution; Sigma, F3777) or rat CD31 antibody (1:200 dilution; BD Biosciences, 553370) in blocking buffer containing 1–5% bovine serum albumin in 0.25–0.5% Triton-X 100 in 1× PBS. The sections were then washed in 0.1 M PBS for 5 min three times and incubated overnight at 4 °C with secondary goat anti-rat antibody conjugated to Alexa Fluor 647 (1:500 dilution; Abcam, ab150159), following by incubation in Hoechst (1:6,000 dilution;) for 7 min and mounting via SlowFade Diamond Antifade Mountant (Invitrogen, S36963). We imaged the stained and mounted brain samples by spinning disc microscopy using a Zeiss CellObserver microscope equipped with Yokogawa spinning disks, Hamamatsu Orca Fusion scientific CMOS camera, and a Fluar ×40/1.20 water immersion objective. We also used ZEISS confocal laser scanning microscope LSM980 and ZEISS Zen Blue 2012 software to image the brain slices. For the green channel (FITC), an illumination wavelength of 488 nm and emission filter BP525/50 were used. For the red channel (DsRed), an illumination wavelength of 561 nm and emission filter BP629/62 were used. For the far-red channel (Alexa Fluor 647), an illumination wavelength of 635 nm and emission filter BP629/62 were used. For the blue channel (Hoechst), an illumination wavelength of 405 nm and emission filter BP450/50 were used. Z-stack images of the continuous vasculature, PA, precapillary sphincters and first-order to third-order capillaries, and if possible higher-order capillaries, were recorded at a resolution of (x) 0.1 μm/pixel × (y) 0.1 μm/pixel × (z-step) 0.28 μm in coronal brain slices from the somatosensory cortex.

Image analysis of immunohistochemistry

In this study, we used the fluorescence intensity of antibodies as a proxy of protein density, that is, αSMA and NG2, and compared them at different orders of capillaries. The existing disadvantage to quantify the protein density in the immunostained brain slices is the uneven fluorescence intensity of antibodies at different depths. This is mainly attributed to: (1) the decline of antibody binding efficacy from surface toward the center of the slice; (2) the excitation laser power is scattered and therefore reduced, when imaging the brain slice from top to bottom. Therefore, we implemented a new image post-processing algorithm to overcome the aforementioned problem. Firstly, an identical background area for every plane was manually selected, avoiding any vessels all through the image stack (Extended Data Fig. 5a). Secondly, we calculated the background mean intensity for each plane, and plotted it with all planes in the z-stack (Extended Data Fig. 5a). Thirdly, we normalized the background intensity to the maximal intensity value in the *z*-stack, by multiplying a weight for the pixel intensity of each plane (Extended Data Fig. 5a). Lastly, the new image stack was flattened by maximal intensity projection (Extended Data Fig. 5a). Furthermore, we used semi-manual customized code to identify the whole vessel surface and pericyte-covered area (Extended Data Fig. 5b). The selected region in the αSMA image was based on the mural cell-covered area in the DsRed image. Mural cell coverage is defined as the percentage of vessel surface area that is covered by somata of and processes originating from the mural cells and based on the NG2-positive area along and around the vessel surface, providing a possible anatomical substrate for control of vessel diameter. The somas of the vascular mural cells were identified by co-staining with DsRed and Hoechst.

Computational modeling

We developed a simple hemodynamic network model based on image reconstruction of a single PA and venule and their associated capillaries. Briefly, Amira software (version 6.1) was used to segment a z-stack of images, preprocessed with a Gaussian filter and background subtraction to facilitate segmentation. Network nodes, edges and vessel lengths and radii were extracted from the reconstruction. However, the vessel radii of the upper PA and the first-order, second-order and third-order capillaries were taken from the original image data and, for each simulation, the vessel radii of specific vessels in the network were deliberately changed. Assuming that the vessels are rigid and the laminar flow (Q), the flow resistance of individual vessel segments was calculated using Poiseuille's law and the standard hemodynamics measure of flow resistance (R): $\Delta P = QR = \frac{8\mu LQ}{\pi r^4}$, that is, $R = \frac{8\mu L}{\pi r^4}$, where P is pressure, μ is dynamic viscosity, L is vessel length, and r is vessel radius. In a network, Kirchoff's law states that the sum of flows entering and leaving any internal node equals zero: $\Sigma_j Q_j = \sum_j \frac{\Delta P_j^n}{R_j^n} = 0$, where Q_j^n is the flow, R_j^n is the vascular flow resistance, and ΔP_j^n is the pressure drop in the j'th vessel entering the n'th node. We applied the empirical model describing the changes in the apparent viscosity of blood (μ) with diameter (D) and hematocrit:

$$C = \left(0.8 + exp^{(-0.075D)}\right) \cdot \left(\frac{1}{1 + 10^{-11} \cdot D^{12}} - 1\right) + \frac{1}{\left(1 + 10^{-11} \cdot D^{12}\right)}$$

$$\mu_{0.45} = 220 \cdot exp^{(-1.3D)} + 3.2 - 2.44exp\left(-0.06D^{0.645}\right)$$

$$\mu = 1 + (\mu_{0.45} - 1)\frac{(1 - H_D)^C - 1}{(1 - 0.45)^C - 1}$$

The discharge hematocrit (H_D) was calculated based on a tube hematocrit (H_T) of 0.3:

$$\frac{H_T}{H_D} = H_D + (1 - H_D)\left(1 + 1.7exp^{(-0.415D)} - 0.6exp^{(-0.011D)}\right)$$

To solve the system of linear equations, we chose the boundary conditions such that the inlet pressure into the PA was 25 mm Hg in the control situation and every outlet pressure of the capillaries was 5 mm Hg. The system was solved using the root solver in SciPy (1.1.0) and Pycharm Community Edition 2020.3.

Limitations

All assumptions underlying Poiseuille's law and Ohmic resistances in laminar flows apply. The boundary conditions strongly influence the solution because the system is forced to comply with the preset boundary pressures. However, the effects of a changing diameter on the pressure and flow within the network are evident. We also assume that the empirical formulas to calculate blood viscosity apply to the cerebral microcirculation of mice.

Statistics and reproducibility

The investigators were not blinded to data collection, but blinded to data analysis. No statistical method was used to predetermine sample size, but our samples sizes are similar to those reported in previous publications[10,11]. Animal experiments that did not show significant vasodilation (<5% diameter change) by WP stimulation at <50% examined vasculatures were terminated and excluded. This reflected a failed craniotomy surgery or bad physiological state of the mouse. Datasets are presented as the mean ± s.e.m. with individual data points. Each experiment at the same location of the same mouse was not repeated to avoid puffing-induced change for resting state. The normality of data was assessed using Shapiro–Wilk and graphical tests. If the data were not normally distributed, the data were log-transformed and retested for normality. Linear mixed-effect model analysis was used. Vessel segments (PA, precapillary sphincters and first-order to third-order capillaries) were defined as the fixed effect, whereas the mouse age and particular vasculature were included as random effects as needed. Significant differences were estimated by likelihood ratio tests of the linear mixed-effect model with the fixed effect in question against a model without the fixed effect. Tukey–Kramer's post hoc test was used for pairwise comparisons between elements in the fixed-effect group. All statistical analyses were performed using R studio (version 3.4.4, packages lme4 and multcomp).

Extended Data

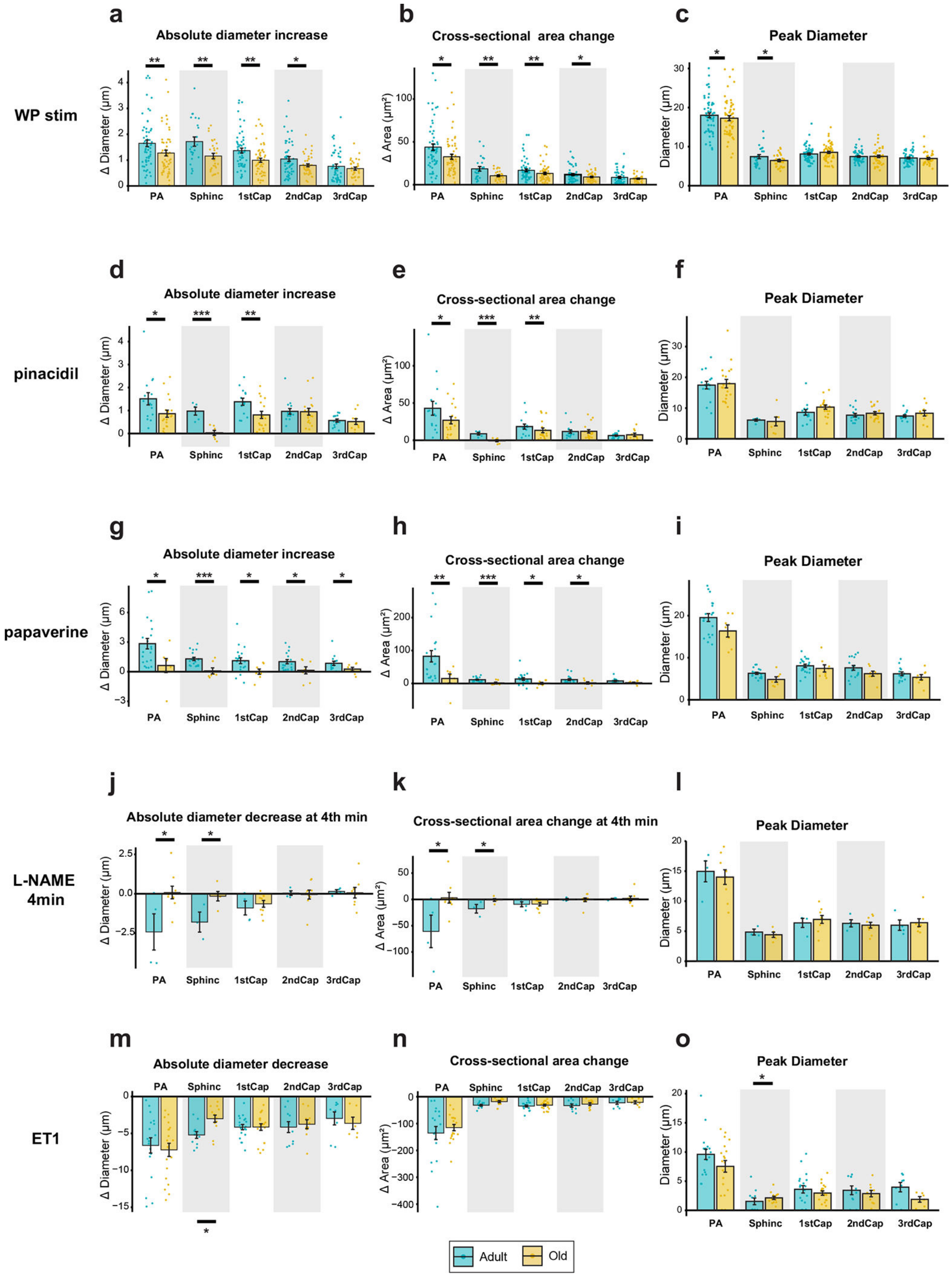

Extended Data Fig. 1 |. Comparison of absolute diameter changes, cross-sectional area changes and peak diameters by different stimulations in adult and old mice.

(**a–c**) Absolute diameter changes, cross-sectional area changes and peak diameters and peak diameters of vasodilation by whisker pad stimulation (WP stim). Adult: N = 17 animals, n = 34 vessels. Old: N = 17 animals, n = 25 vessels. (**d–f**) Absolute diameter changes, cross-sectional area changes and peak diameters and peak diameters of vasodilation by K_{ATP} channel opener pinacidil puff. Adult: N = 9 animals, n = 15 vessels. Old: N = 11 animals, n = 17 vessels. (**g–i**) Absolute diameter changes, cross-sectional area changes and peak diameters and peak diameters of vasodilation by papaverine puff. Adult: N = 8 animals, n = 17 vessels. Old: N = 5 animals, n = 8 vessels. (**j–l**) Absolute diameter changes, cross-sectional area changes and peak diameters and peak diameters of vasoconstriction by L-NAME intravenous infusion (4 min post). Adult: N = 5 animals, n = 5 vessels. Old: N = 8 animals, n = 8 vessels. (**m–o**) Absolute diameter changes, cross-sectional area changes and peak diameters and peak diameters of vasoconstriction by ET1 puff. Adult: N = 5 animals, n = 10 vessels. Old: N = 7 animals, n = 15 vessels. Linear mixed effect models were used to test for differences among vessel segments, followed by Tukey post hoc tests for pairwise comparisons. Data are given as mean ± SEM. * indicates $p < 0.05$, ** indicates $p < 0.01$, *** indicates $p < 0.001$.

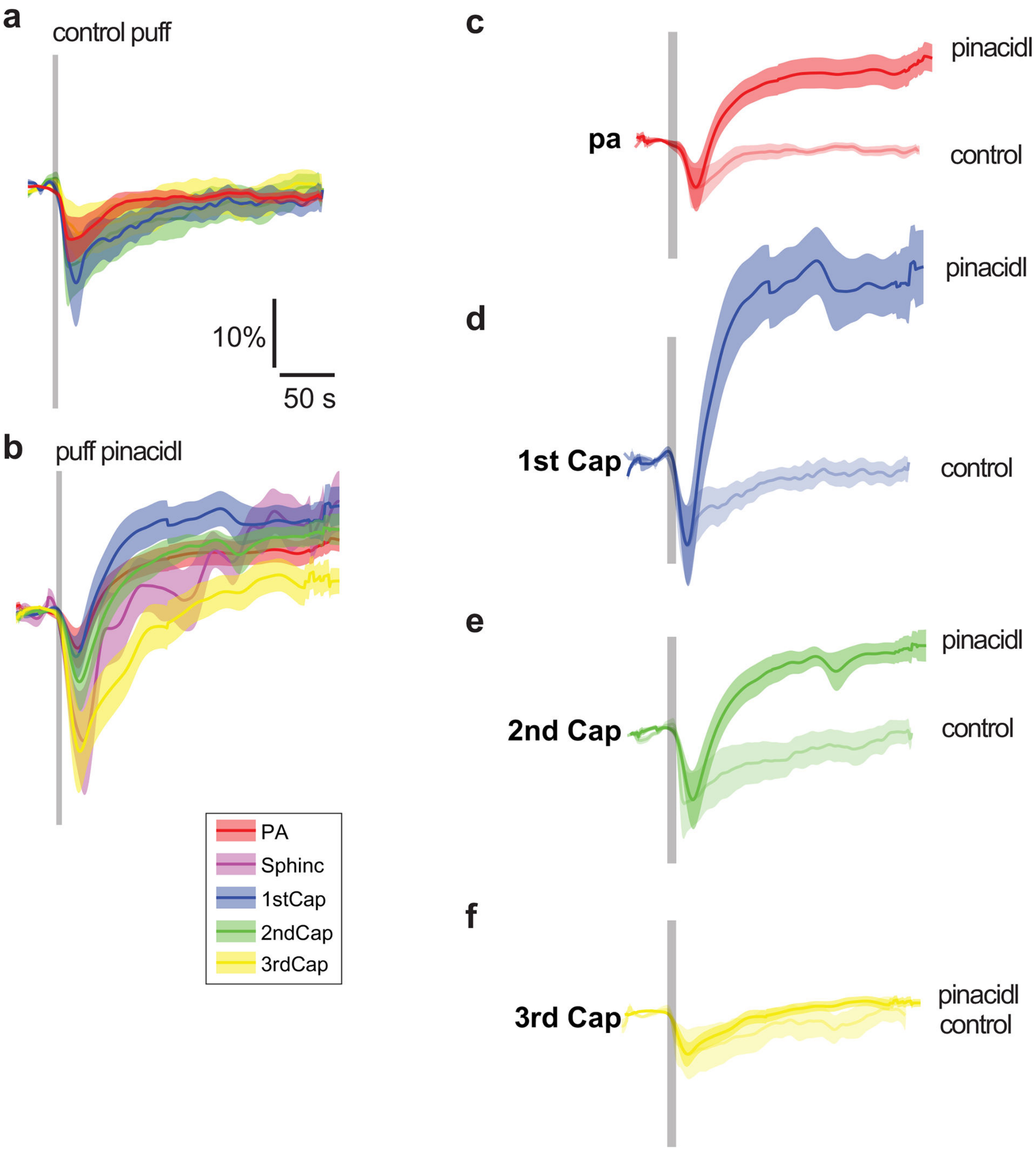

Extended Data Fig. 2 |. Comparison of control puff and pinacidil puff.

The control puff experiments were performed with the same concentration of fluorescent dye but without an active compound. The initial 'constricting' artifact can be perfectly overlaid by both control puff and pinacidil puff, using the time of puffing as a time lock and normalizing the negative peak at the moment of puffing. (**a**) Vessel diameter change by control puff. (**b**) Vessel diameter change by pinacidil puff. (**c-f**) Overlay of the vessel diameter change curves at each capillary order, with (**c**) as penetrating arteriole, (**d**) as 1st order capillary, (**e**) as 2nd order capillary and (**f**) as 3rd order capillary. Data are given as mean ± SEM.

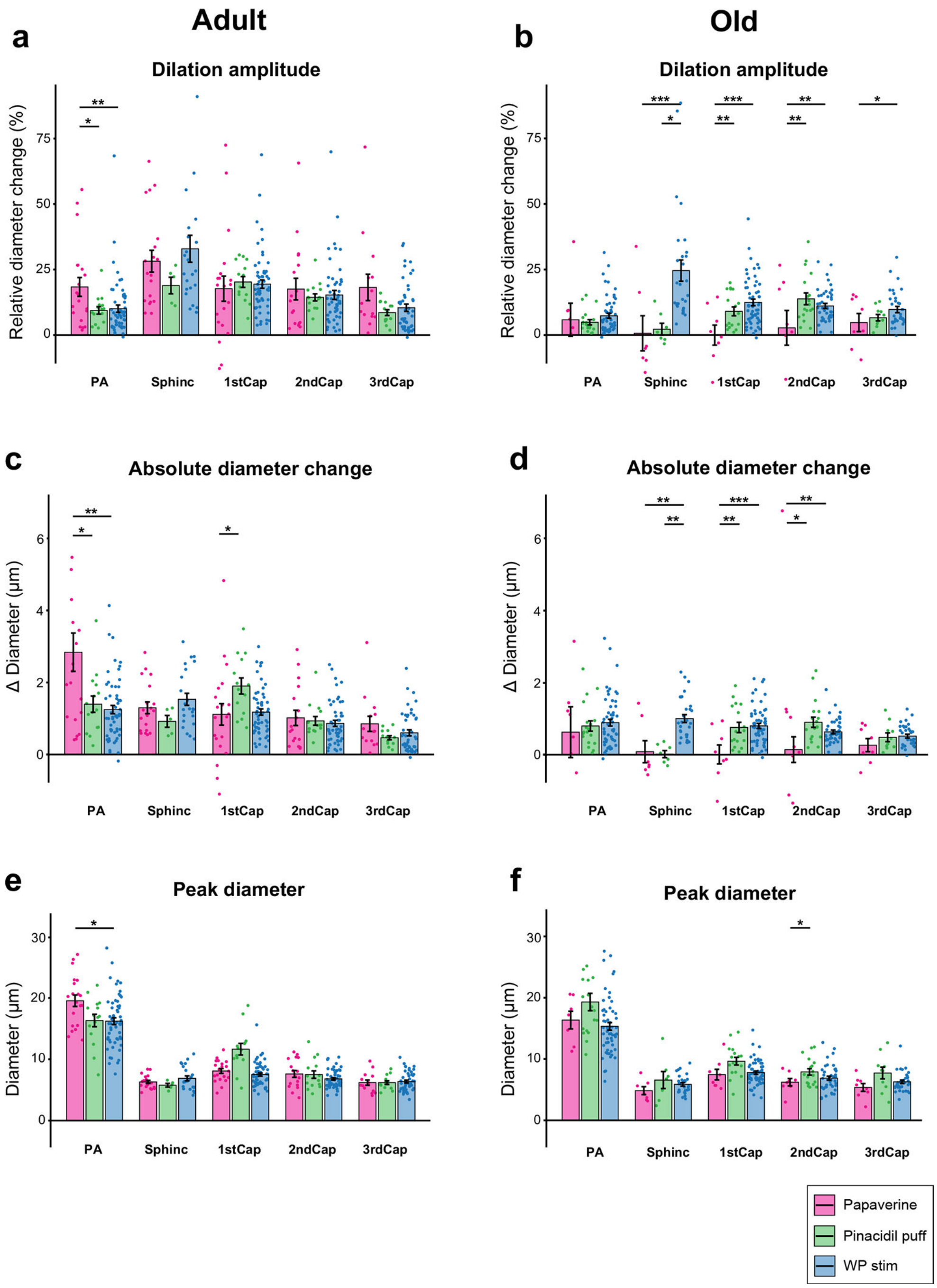

Extended Data Fig. 3 |. Comparison of vasodilation elicited by papaverine puff, pinacidil puff, and whisker pad (WP) stimulation.

(**a–b**) Relative diameter change elicited by the three stimulations in (**a**) adult and (**b**) old mice. (**c–d**) Absolute diameter change elicited by the three stimulations in (**c**) adult and (**d**) old mice. (**e–f**) Peak diameter elicited by the three stimulations in (**e**) adult and (**f**) old mice. WP stimulation: Adult: N = 31 animals, n = 56 vessels. Old: N = 26 animals, n = 53 vessels. Pinacidil: Adult: N = 9 animals, n = 15 vessels. Old: N = 11 animals, n = 17 vessels. Papaverine: Adult: N = 8 animals, n = 17 vessels. Old: N = 5 animals, n = 8 vessels. Linear mixed effect models were used to test for differences among vessel segments, followed by Tukey post hoc tests for pairwise comparisons. Data are given as mean ± SEM. * indicates $p < 0.05$, ** indicates $p < 0.01$, *** indicates $p < 0.001$.

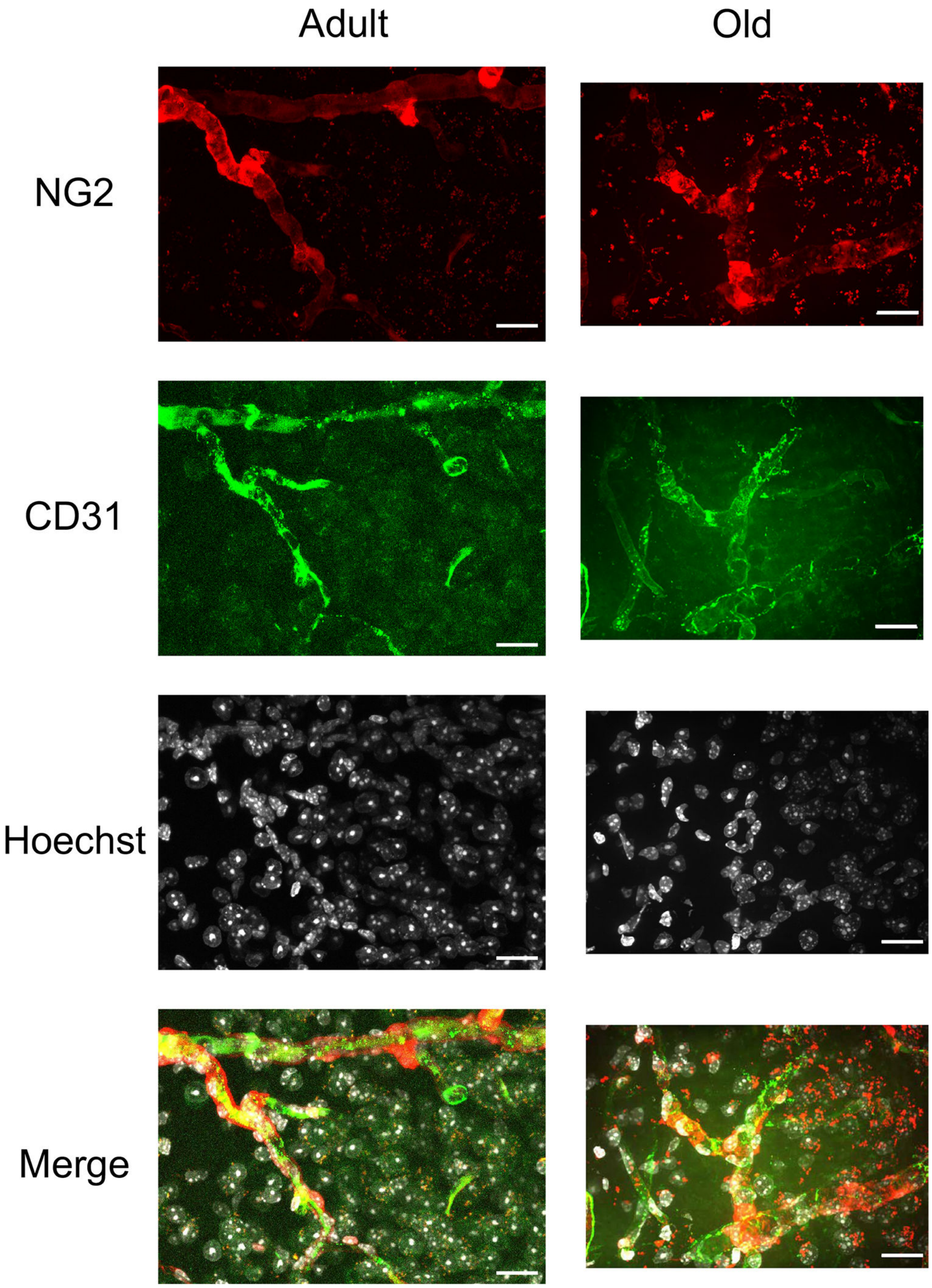

Extended Data Fig. 4 |. Representative immunohistochemical images of staining CD31 and Hoechst in the adult and old mouse brains.

This is to identify the vascular endothelial cell somata. Maximum intensity projection of an (left) adult and (right) old brain image stack. Red: NG2; Green: CD31; Gray: Hoechst. Scale bar: 20 µm.

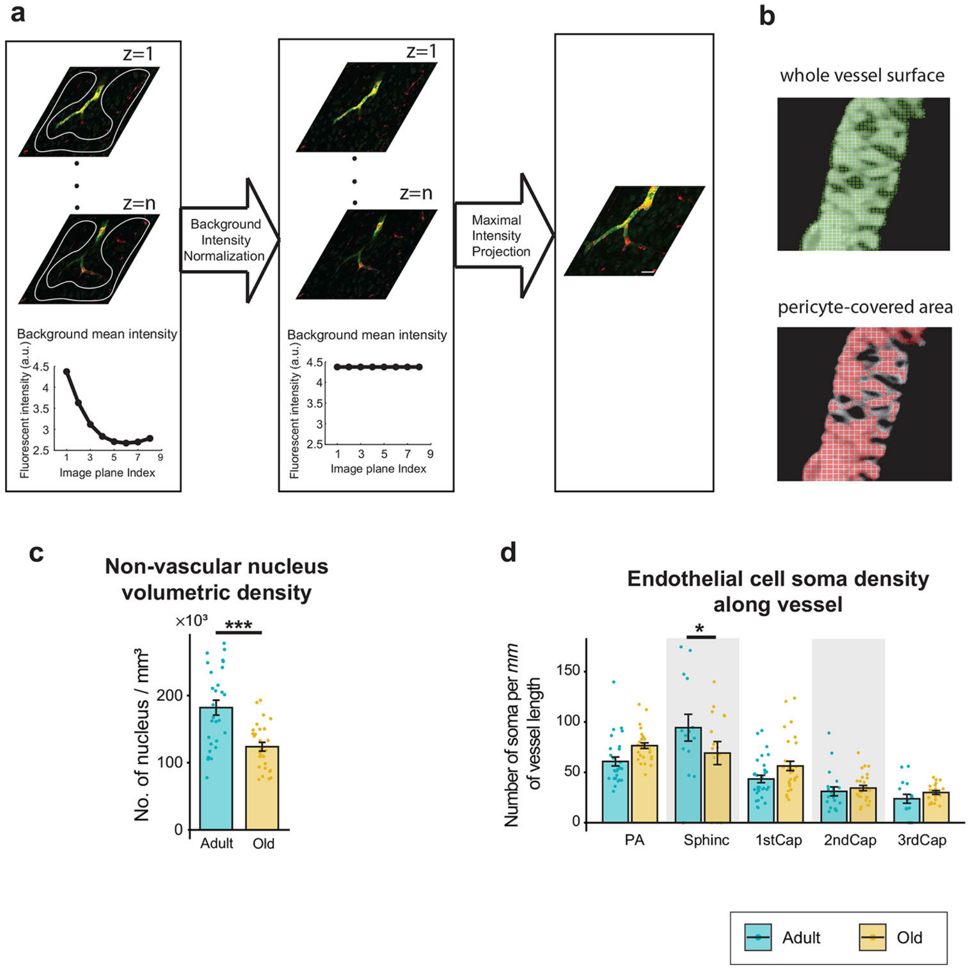

Extended Data Fig. 5 |. Immunohistochemical analysis of mural cell structural change with age. (**a**) Image processing procedure for the z-stack was to free-hand draw the background area and then calculate the mean background fluorescence intensity for each image plane. The background intensity was normalized to the peak value of the z-stack. Finally, the z-stack images were projected onto one image by maximal projection. (**b**) The semi-manual customized code is to identify the whole vessel surface and pericyte-covered area. Upper: Hand-drawn delineation of the vessel region in the green and red imags. Lower: The NG2 image was used to select the mural cell-positive pixels. (**c**) Non-vascular nucleus volumetric density. The non-vascular nucleus is defined as nuclei with a distance to the nearby vessels. (**d**) Endothelial cell soma density obtained by dividing the number of endothelial cell somas and the examined vessel length. Adult: N = 3 animals, n = 25 vessels. Old: N = 3 animals, n = 26 vessels. Linear mixed effect models were used to test for differences among vessel segments, followed by Tukey post hoc tests for pairwise comparisons. Data are given as mean ± SEM. * indicates $p < 0.05$, **indicates $p < 0.01$, ***indicates $p < 0.001$.

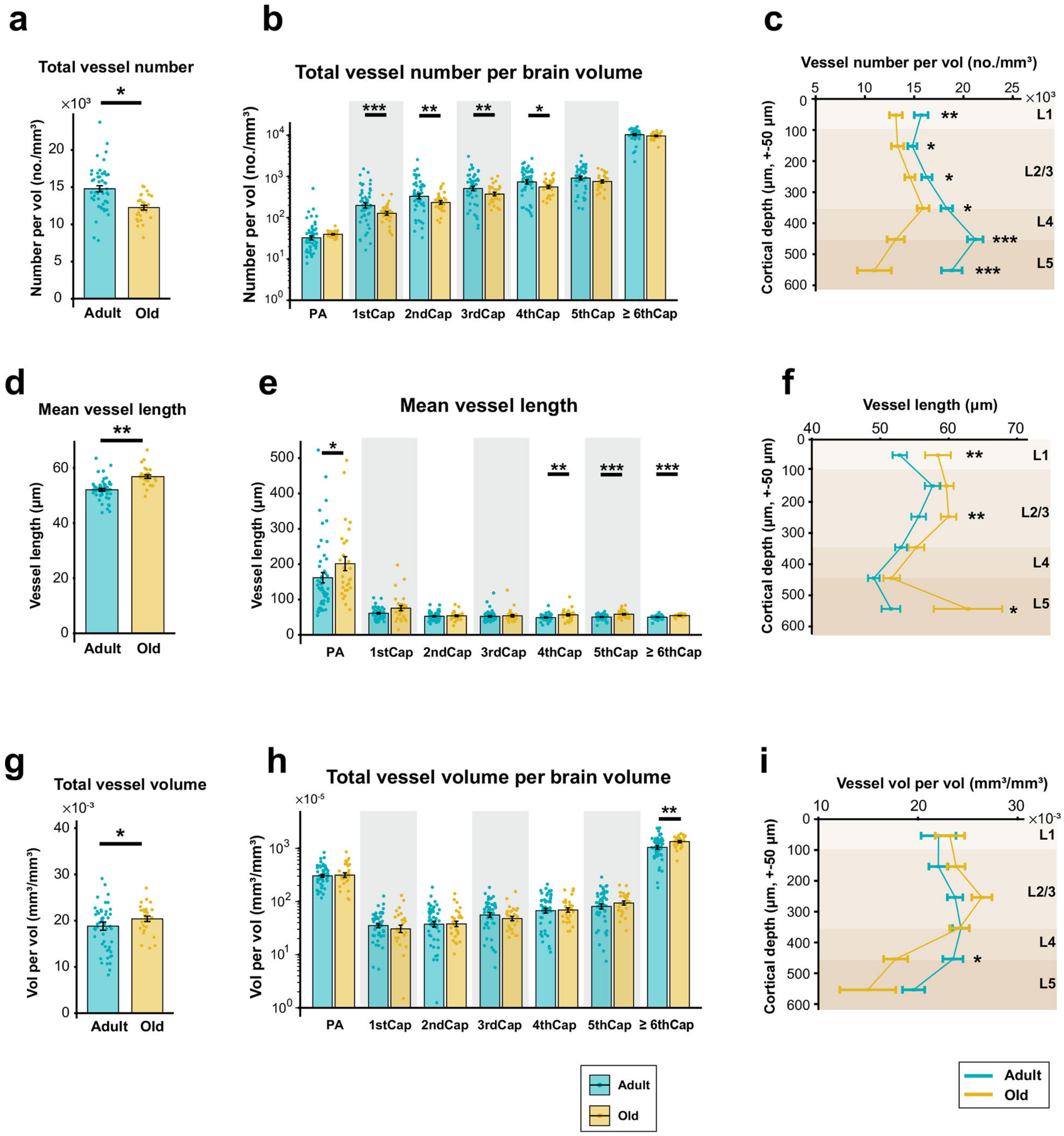

Extended Data Fig. 6 |. *In vivo* vascular structural changes with aging.

(**a–c**) Total vessel number per brain volume in adult and old somatosensory cortex. (**a**) General total vessel number, (**b**) capillary order dependent total vessel number, and (**c**) cortical depth dependent total vessel number. (**d–f**) Mean vessel length in adult and old somatosensory cortex. (**d**) General mean vessel length, (**e**) capillary order dependent mean vessel length, and (**f**) cortical depth dependent mean vessel length. (**g–i**) Total vessel volume per brain volume in adult and old somatosensory cortex. (**g**) General total vessel volume, (**h**) capillary order dependent total vessel volume, and (**i**) cortical depth dependent total vessel volume. Adult: N = 6 animals, n = 52 vessels. Old: N = 4 animals, n = 29 vessels. Linear mixed effect models were used to test for differences among vessel segments, followed by Tukey post hoc tests for pairwise comparisons. Data are given as mean ± SEM. * indicates $p < 0.05$, ** indicates $p < 0.01$, ***indicates $p < 0.001$. L1–L5 denote cortical sublayers.

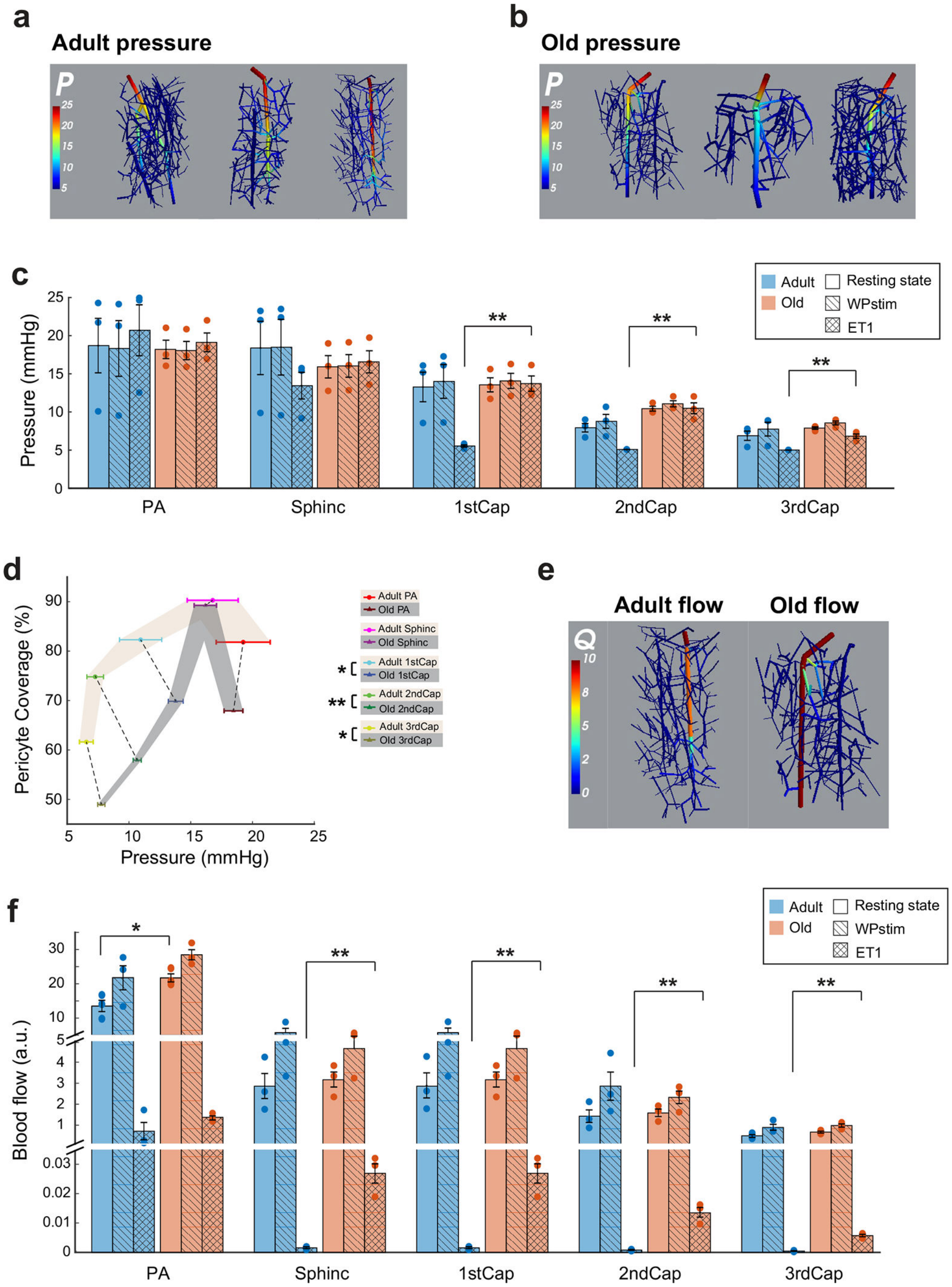

Extended Data Fig. 7 |. Math modeling indicates that vascular blood flow and pressure are affected by aging.

(**a–b**) Mathematical modeling of pressure distribution in 3D reconstructed vasculature from 3 adult (**a**) and 3 old (**b**) mouse brains. (**c**) Summary of the averaged pressures in penetrating arteriole (PAs), precapillary sphincters, and first- to third-order capillaries in the vascular networks under resting-state, with whisker pad stimulation (WPstim), and after ET1 puff. (**d**) Correlation of mural cell coverage and blood pressure summarized for all three states. The dashed line connects the adult and old measurements at the same vascular segment for easy comparison. (**e**) Mathematical modeling of flow distribution in 3D reconstructed vasculature from 3 adult and 3 old mouse brains. Only one representative image from each group is shown. (**f**) Summary of the average flow in PAs, precapillary sphincters, and first- to third-order capillaries in the vascular networks under resting-state, WP stim, and after ET1 puff. Adult: N = 3 animals, n = 3 vessels; Old: N = 3 animals, n = 3 vessels. Linear mixed effect models were used to test for differences among vessel segments, followed by Tukey post hoc tests for pairwise comparisons. Data are given as mean ± SEM. * indicates $p < 0.05$, ** indicates $p < 0.01$, *** indicates $p < 0.001$.

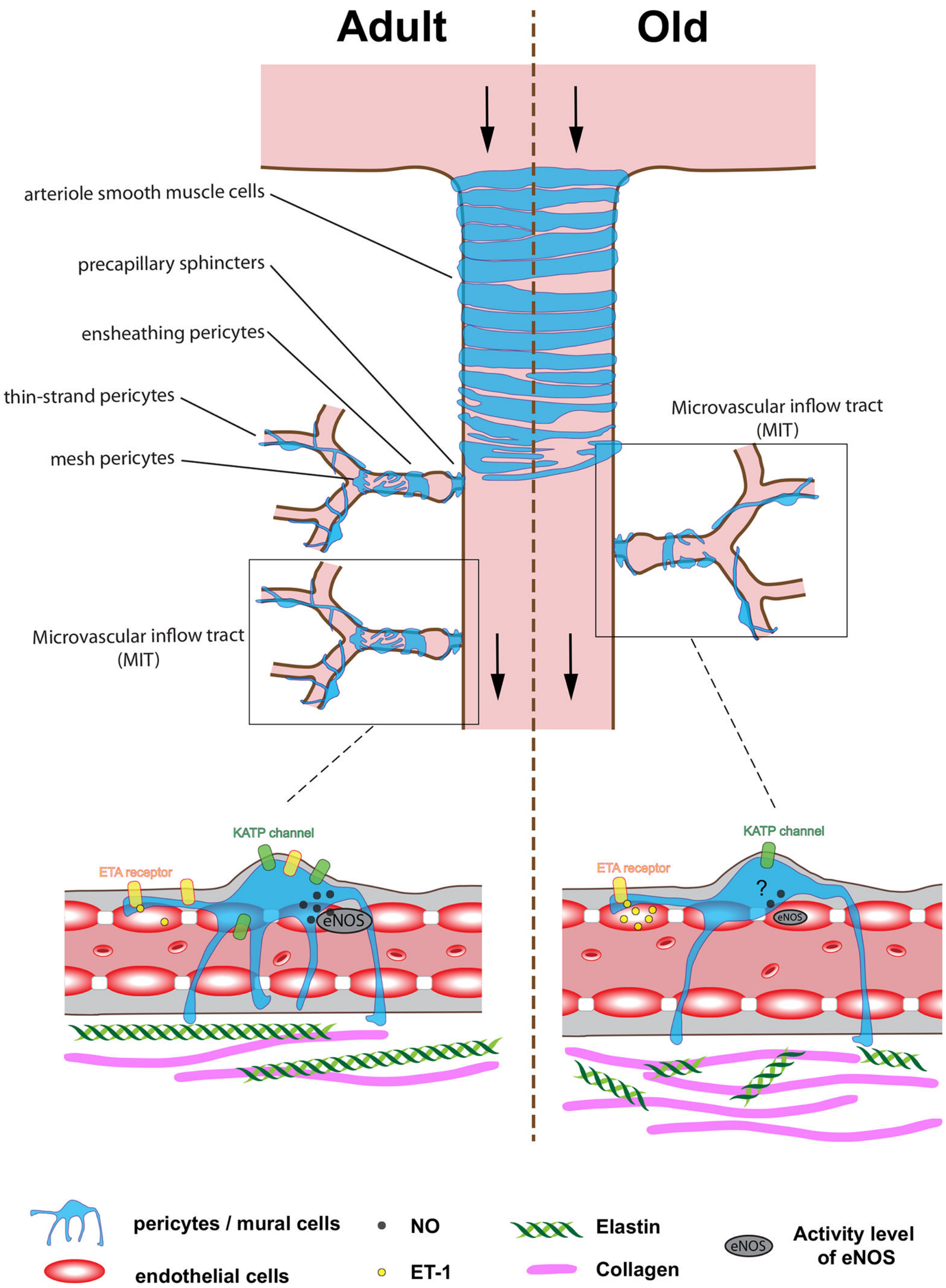

Extended Data Fig. 8 |. Diagram of vascular mural cell phenotypes at the microvascular inflow tract (MIT) and the mechanisms that contribute to changes in function and morphology with MIT aging.

(1) Vascular mural cell phenotypes at the MIT. Arteriole vascular smooth muscle cells (VSMCs) have spindle-shaped cell bodies. Like contractile bands, they cover the circumferences of the penetrating arterioles in a single layer. We previously reported the existence of precapillary sphincters displaying indentation of the vessel lumen and strong expression of αSMA at 50% of the joints between penetrating arterioles and first-order capillaries. They are important in maintaining and regulating capillary blood

flow. Ensheathing pericytes cover capillaries up to the third order. Ensheathing pericytes have short longitudinal processes with dense circumferential offshoots woven together to create a meshed circumferential coverage of the capillary that covers 95% of the capillary endothelium. VSMCs, precapillary sphincters and ensheathing pericytes do express αSMA. A stepwise decrease in αSMA content is observed along the first, second, third, and up to the fourth order of capillary. This αSMA-positive arteriole-proximal capillary segment is termed the microvascular inflow tract (MIT)—here, the pericyte coverage across capillary junctions is ~90%; further downstream, the capillary junctional pericyte coverage is ~45%. Mesh pericytes exhibit mesh-like morphology and are found downstream of ensheathing pericytes and the αSMA terminus; they have lesser endothelial coverage (71.6%) than ensheathing pericytes, and their longitudinal processes are longer and have a less dense network of circumferential offshoots. In higher-order capillaries, thin-strand pericytes display thin and long longitudinal processes, with only a few circumferential offshoots that extend along and cover 51.3% of the capillary endothelium. (2) Changes in morphology and signaling investigated in this study contribute to vascular aging at the MIT. The resting-state diameter of vessels at the MIT increases with age, but the coverage by mural cells decreases. K_{ATP} channels are downregulated and are less densely expressed by aging. The probability of K_{ATP}-channel opening is also reduced with age. NO production and bioavailability maybe reduced by aging, and our results suggest that ongoing NO-dependent mechanisms are attenuated in old mice. Although ET1 signaling and synthesis are increased in old relative to adult mice, ETA receptors are downregulated with age. Furthermore, aging is accompanied by fragmented elastin, deposition of collagens, and vessel stiffness. All the above age-related changes at the MIT contribute to reduced responsivity to both vasodilators and vasoconstrictors, indicating the existence of a compensating mechanism to keep cerebral blood flow and oxygen supply at a physiologically healthy level with healthy aging.

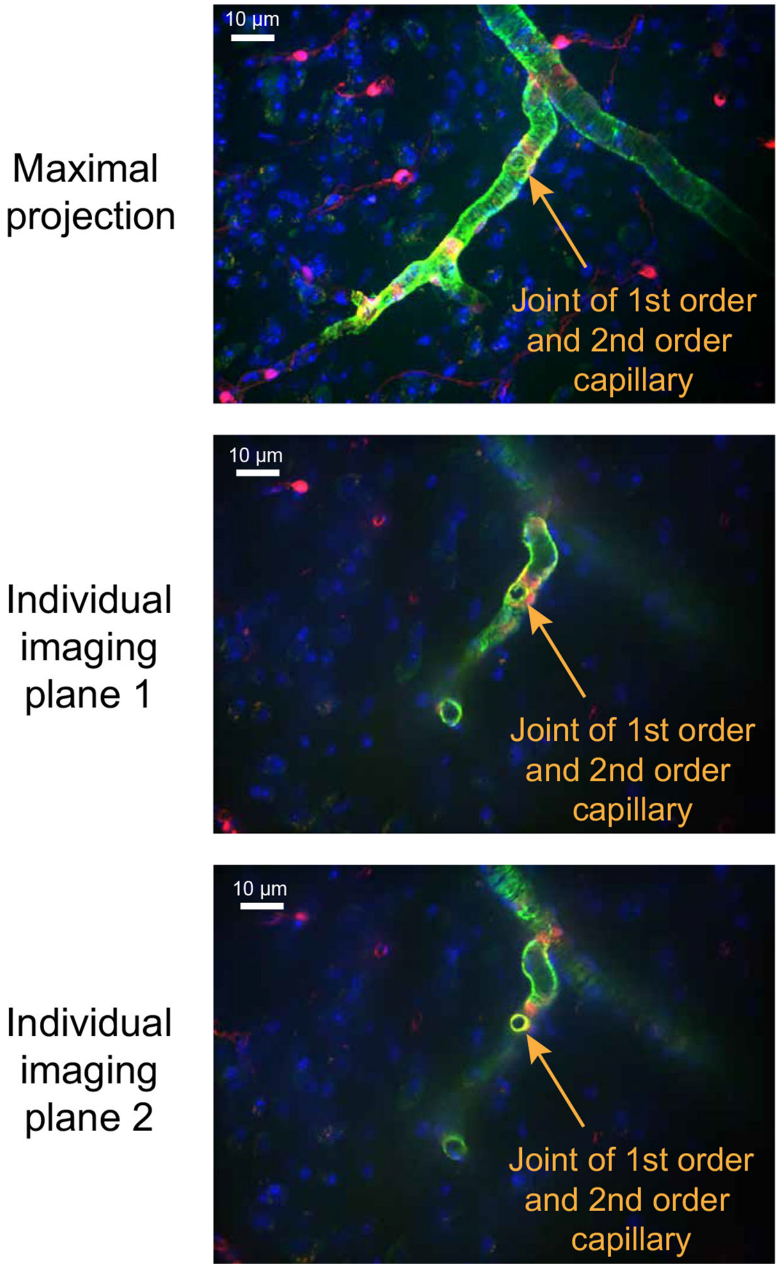

Extended Data Fig. 9 |. Max projection and individual planes in Fig. 3a.

The joint of 1st and 2nd order capillary in Fig. 3a can be identified by examining individual planes.

Extended Data Table 1 |

The vessel diameters, dilation and constriction amplitudes used in the mathematical modeling

	Resting state diamete (μm)		**Whisker pad stimulation induced peak dilation (%)**		**ET1 puffing induced peak constriction (%)**	
	Adult	**Old**	**Adult**	**Old**	**Adult**	**Old**
Penetrating arterioles	14.2114	14.62536	10.228421	6.860536	−39.47547	−49.97799
Sphincters	4.680909	4.858621	34.02045	19.46862	−80.64468	−56.80134
1st order capillaries	6.15375	7.130357	19.90661	12.5075	−57.80691	−58.14957
2nd order capillaries	5.8606	6.482326	16.7312	11.12442	−55.91794	−57.0615
3rd order capillaries	5.617174	5.798485	11.582174	9.784848	−41.94744	−63.22993

They are based on the two-photon measurements in this study.

Supplementary Material

Refer to Web version on PubMed Central for supplementary material.

Acknowledgements

We acknowledge Niels Bohr Institute Electronics & Mechanical Workshop, University of Copenhagen, where we receive great technical support from S. Stausgaard-Petersen, J. H. Fagerlund and their colleagues. We acknowledge the Core Facility for Integrated Microscopy, Faculty of Health and Medical Sciences, University of Copenhagen, where we used spinning disc confocal microscopy in our in vitro studies. This study was supported by the Lundbeck Foundation (R273-2017-1791 and R345-2020-1440), the Danish Medical Research Council (1133-00016A), the Alice Brenaa Foundation, Augustinus Foundation (19-2858), Carl og Ellen Hertz Familielegat (19.19.2), A. P. Møller Foundation (20-L-0243), Helsefonden (21-B-0441), the Novo Nordisk foundation (0064289) and a Nordea Foundation Grant to the Center for Healthy Aging (02-2017-1749).

Data availability

The source data and custom code are available in public repository G-Node: https://doi.org/10.12751/g-node.zcg4cy/.

References

1. Aanerud J et al. Brain energy metabolism and blood flow differences in healthy aging. J. Cereb. Blood Flow Metab. 32, 1177–1187 (2012). [PubMed: 22373642]
2. Moeini M et al. Compromised microvascular oxygen delivery increases brain tissue vulnerability with age. Sci. Rep. 8, 8219 (2018). [PubMed: 29844478]
3. De Silva TM & Faraci FM Contributions of aging to cerebral small vessel disease. Annu. Rev. Physiol. 82, 275–295 (2020). [PubMed: 31618600]
4. Chen JJ Functional MRI of brain physiology in aging and neurodegenerative diseases. NeuroImage 187, 209–225 (2019). [PubMed: 29793062]
5. Esopenko C & Levine B Aging, neurodegenerative disease, and traumatic brain injury: the role of neuroimaging. J. Neurotrauma 32, 209–220 (2015). [PubMed: 25192426]
6. Chen R-L, Balami JS, Esiri MM, Chen L-K & Buchan AM Ischemic stroke in the elderly: an overview of evidence. Nat. Rev. Neurol. 6, 256–265 (2010). [PubMed: 20368741]

7. Bell RD et al. Pericytes control key neurovascular functions and neuronal phenotype in the adult brain and during brain aging. Neuron 68, 409–427 (2010). [PubMed: 21040844]
8. Grant RI et al. Organizational hierarchy and structural diversity of microvascular pericytes in adult mouse cortex. J. Cereb. Blood Flow Metab. 39, 411–425 (2019). [PubMed: 28933255]
9. Hall CN et al. Capillary pericytes regulate cerebral blood flow in health and disease. Nature 508, 55–60 (2014). [PubMed: 24670647]
10. Grubb S et al. Precapillary sphincters maintain perfusion in the cerebral cortex. Nat. Commun. 11, 395 (2020). [PubMed: 31959752]
11. Zambach SA et al. Precapillary sphincters and pericytes at first-order capillaries as key regulators for brain capillary perfusion. Proc. Natl Acad. Sci. USA 118, e2023749118 (2021). [PubMed: 34155102]
12. West KL et al. BOLD hemodynamic response function changes significantly with healthy aging. NeuroImage 188, 198–207 (2019). [PubMed: 30529628]
13. Diaz-Otero JM, Garver H, Fink GD, Jackson WF & Dorrance AM Aging is associated with changes to the biomechanical properties of the posterior cerebral artery and parenchymal arterioles. Am. J. Physiol. Heart Circ. Physiol. 310, H365–H375 (2016). [PubMed: 26637558]
14. Fonck E et al. Effect of aging on elastin functionality in human cerebral arteries. Stroke 40, 2552–2556 (2009). [PubMed: 19478233]
15. Bolton TB Mechanisms of action of transmitters and other substances on smooth muscle. Physiol. Rev. 59, 606–718 (1979). [PubMed: 37533]
16. Boswell-Smith V, Spina D & Page CP Phosphodiesterase inhibitors. Br. J. Pharmacol. 147, S252–S257 (2006). [PubMed: 16402111]
17. Chappie TA, Helal CJ & Hou X Current landscape of phosphodiesterase 10A (PDE10A) inhibition. J. Med. Chem. 55, 7299–7331 (2012). [PubMed: 22834877]
18. Mandalà M, Pedatella AL, Morales Palomares S, Cipolla MJ & Osol G Maturation is associated with changes in rat cerebral artery structure, biomechanical properties and tone. Acta Physiol. 205, 363–371 (2012).
19. Toth P et al. Resveratrol treatment rescues neurovascular coupling in aged mice: role of improved cerebromicrovascular endothelial function and downregulation of NADPH oxidase. Am. J. Physiol. Heart. Circ. Physiol. 306, H299–H308 (2014). [PubMed: 24322615]
20. Faraci FM, Brian JE Jr & Heistad DD. Response of cerebral blood vessels to an endogenous inhibitor of nitric oxide synthase. Am. J. Physiol. 269, H1522–H1527 (1995). [PubMed: 7503244]
21. Davenport AP et al. Endothelin. Pharmacol Rev. 68, 357–418 (2016). [PubMed: 26956245]
22. Bennett HC & Kim Y Pericytes across the lifetime in the central nervous system. Front. Cell Neurosci. 15, 627291 (2021). [PubMed: 33776651]
23. Ximerakis M et al. Single-cell transcriptomic profiling of the aging mouse brain. Nat. Neurosci. 22, 1696–1708 (2019). [PubMed: 31551601]
24. Kirst C et al. Mapping the fine-scale organization and plasticity of the brain vasculature. Cell 180, 780–795 (2020). [PubMed: 32059781]
25. Young AP et al. Endothelin B receptor dysfunction mediates elevated myogenic tone in cerebral arteries from aged male Fischer 344 rats. Geroscience 43, 1447–1463 (2021). [PubMed: 33403617]
26. Springo Z et al. Aging impairs myogenic adaptation to pulsatile pressure in mouse cerebral arteries. J. Cereb. Blood Flow Metab. 35, 527–530 (2015). [PubMed: 25605292]
27. Toth P et al. Age-related autoregulatory dysfunction and cerebromicrovascular injury in mice with angiotensin II-induced hypertension. J. Cereb. Blood Flow Metab. 33, 1732–1742 (2013). [PubMed: 23942363]
28. Ranki HJ, Crawford RM, Budas GR & Jovanovic A Ageing is associated with a decrease in the number of sarcolemmal ATP-sensitive K^+ channels in a gender-dependent manner. Mech. Ageing Dev. 123, 695–705 (2002). [PubMed: 11850031]
29. Tricarico D & Camerino DC ATP-sensitive K^+ channels of skeletal muscle fibers from young adult and aged rats: possible involvement of thiol-dependent redox mechanisms in the age-related

modifications of their biophysical and pharmacological properties. Mol. Pharmacol. 46, 754–761 (1994). [PubMed: 7969056]

30. Taddei S et al. Age-related reduction of NO availability and oxidative stress in humans. Hypertension 38, 274–279 (2001). [PubMed: 11509489]
31. Donato AJ et al. Vascular endothelial dysfunction with aging: endothelin-1 and endothelial nitric oxide synthase. Am. J. Physiol. Heart. Circ. Physiol. 297, H425–H432 (2009). [PubMed: 19465546]
32. Van Der Loo B et al. Enhanced peroxynitrite formation is associated with vascular aging. J. Exp. Med. 192, 1731–1744 (2000). [PubMed: 11120770]
33. Cernadas MAR et al. Expression of constitutive and inducible nitric oxide synthases in the vascular wall of young and aging rats. Circ. Res. 83, 279–286 (1998). [PubMed: 9710120]
34. Van Guilder GP, Westby CM, Greiner JJ, Stauffer BL & Desouza CA Endothelin-1 vasoconstrictor tone increases with age in healthy men but can be reduced by regular aerobic exercise. Hypertension 50, 403–409 (2007). [PubMed: 17576858]
35. Del Ry S, Maltinti M, Giannessi D, Cavallini G & Bergamini E Age-related changes in endothelin-1 receptor subtypes in rat heart. Exp. Aging Res. 34, 251–266 (2008). [PubMed: 18568982]
36. Ungvari Z, Tarantini S, Donato AJ, Galvan V & Csiszar A Mechanisms of vascular aging. Circ. Res. 123, 849–867 (2018). [PubMed: 30355080]
37. Castelli V et al. Neuronal cells rearrangement during aging and neurodegenerative disease: metabolism, oxidative stress and organelles Dynamic. Front. Mol. Neurosci. 12, 132 (2019). [PubMed: 31191244]
38. Banks WA, Reed MJ, Logsdon AF, Rhea EM & Erickson MA Healthy aging and the blood–brain barrier. Nature Aging 1, 243–254 (2021). [PubMed: 34368785]
39. Nikolakopoulou AM et al. Pericyte loss leads to circulatory failure and pleiotrophin depletion causing neuron loss. Nat. Neurosci. 22, 1089–1098 (2019). [PubMed: 31235908]

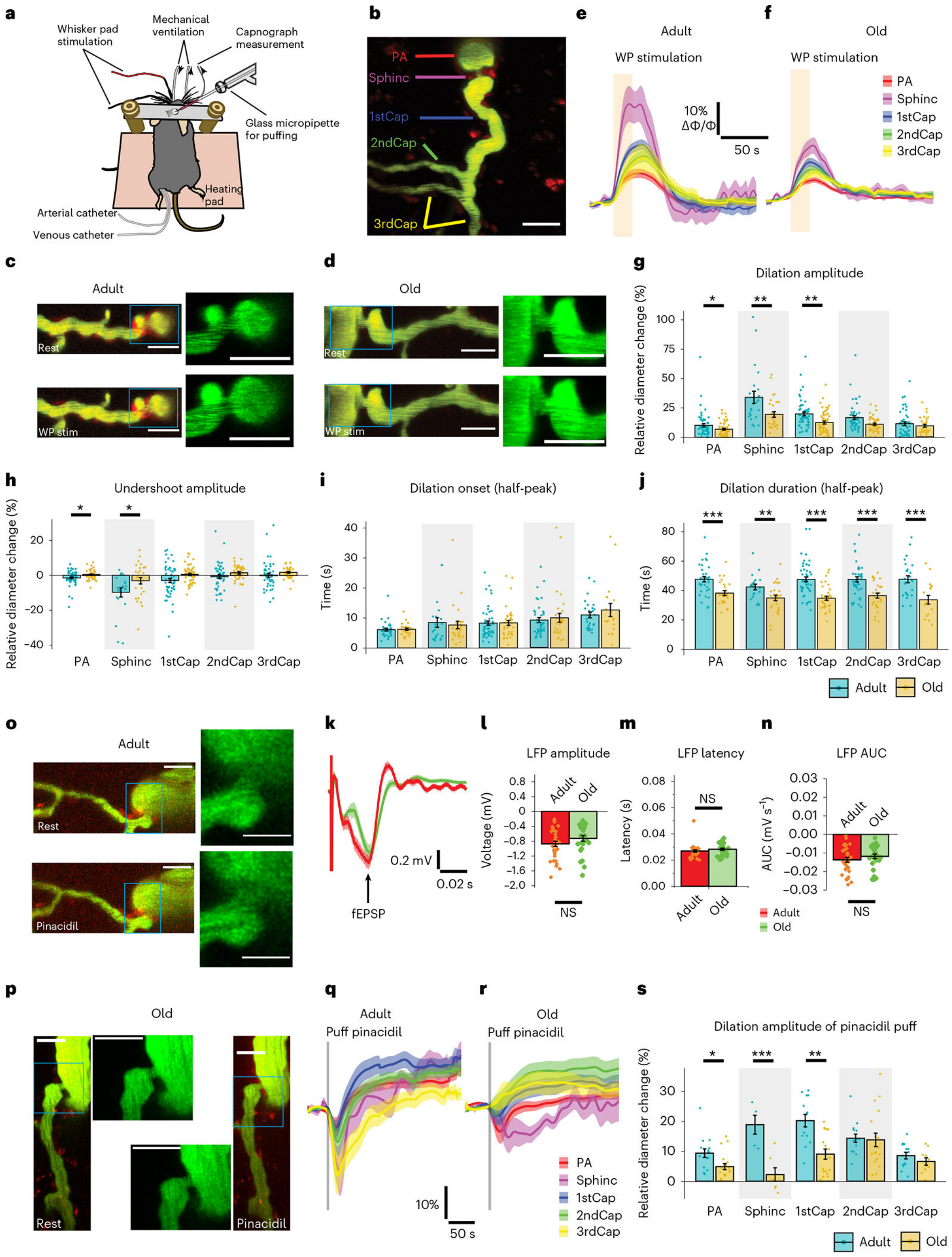

Fig. 1 |. Whisker-pad stimulation-induced and pinacidil-induced vasodilations are reduced in aging and are vascular mural cell dependent.

a, Diagram of the in vivo experimental setup. The physiological state of the mouse was monitored throughout the experiment, including arterial blood pressure, exhaled CO_2, body temperature, heart rate and O_2 saturation. Two stimulations were used: WP stimulation and a glass micropipette inserted into the target area for local ejection (puff). **b**, A two-photon image obtained by maximum intensity projection of a local image stack at MIT, containing the PA, precapillary sphincter (Sphinc), and first-order to third-order capillaries (1stCap, 2ndCap, 3rdCap). Scale bar, 10 µm. **c**,**d**, Representative images of MIT in response to WP stimulation in adult (**c**) and old (**d**) mice. Scale bar, 20 µm. Small insets show enlarged precapillary sphincters (Scale bar, 10 µm.). **e**,**f**, Mean (solid curve) and s.e.m. (shadow) traces of the vessel diameter change at each vessel location upon WP stimulation in adult and old mice. **g–j**, Comparison of relative dilation amplitude (**g**), undershoot amplitude (**h**), half-peak dilation onset (**i**) and half-peak dilation duration (**j**) in adult and old brains. Adult, $N = 31$ animals, $n = 56$ vessels; old, $N = 26$ animals, $n = 53$ vessels. **k**, Elicited LFPs by WP stimulation and recorded by the same glass micropipette. Mean (solid curve) and s.e.m. (shadow) traces of LFPs in adult and old mice. **l–n**, Comparison of the amplitudes, latency and area under the curve (AUC) of fEPSPs. Adult, $N = 17$ animals, $n = 34$ vessels; old, $N = 17$ animals, $n = 25$ vessels. **o**,**p**, Representative images of MIT in response to 5 mM pinacidil puffing in adult and old mice. Scale bar, 20 µm. Small insets show enlarged precapillary sphincters (Scale bar, 10 µm). **q**,**r**, Mean (solid curve) and s.e.m. (shadow) traces of the vessel diameter change at each vessel location upon pinacidil puffing in adult and old mice. **s**, Comparison of relative dilation amplitude by pinacidil puffing. Adult, $N = 9$ animals, $n = 15$ vessels; old, $N = 11$ animals, $n = 17$ vessels. Raw data for pinacidil puffing in adult brains were reused from our previous publication[11]. Linear mixed-effect models were used to test for differences among vessel segments, followed by Tukey post hoc tests for pairwise comparisons. Data are given as the mean ± s.e.m. $^{*}P < 0.05$, $^{**}P < 0.01$, $^{***}P < 0.001$. NS, not significant.

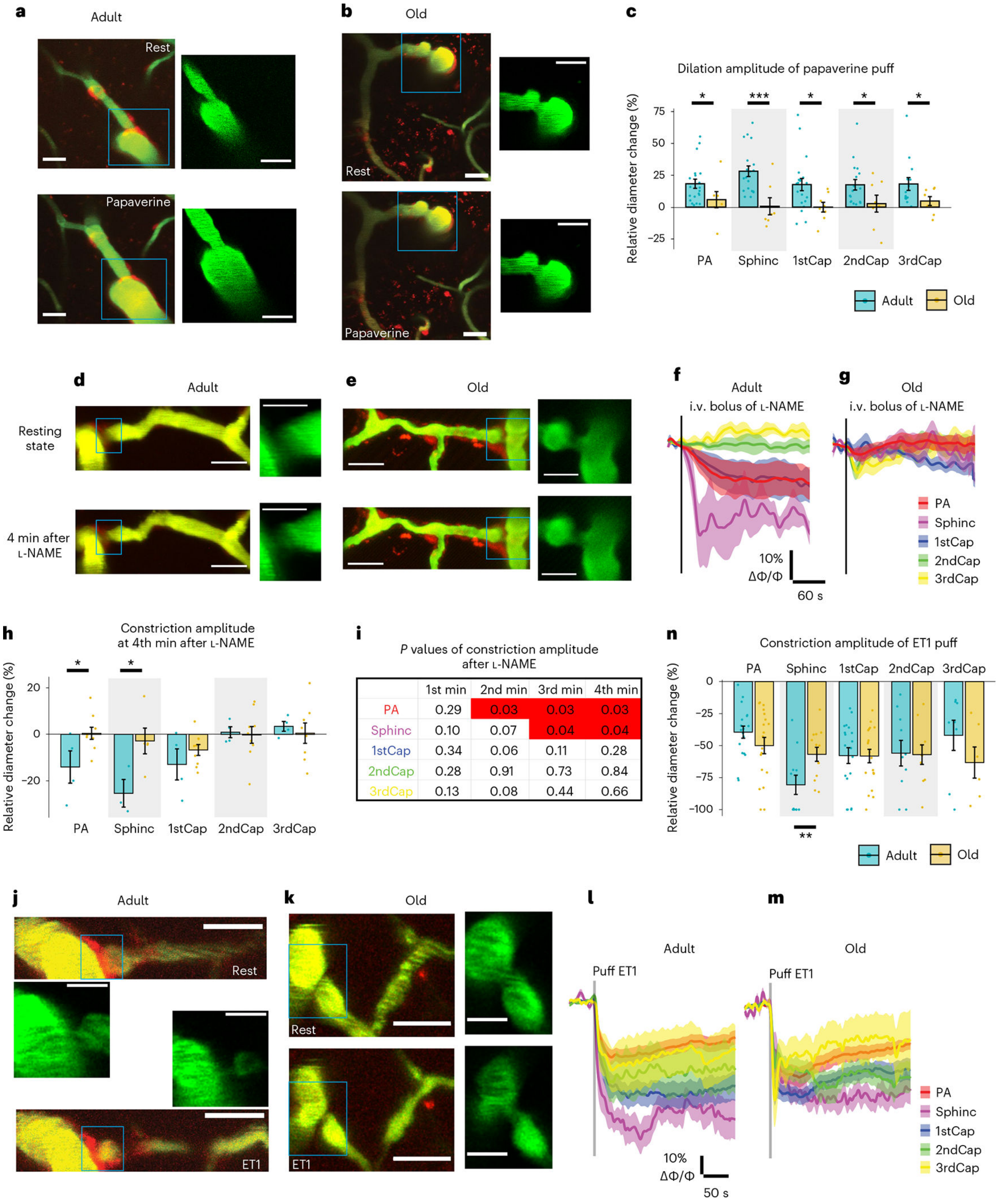

	1st min	2nd min	3rd min	4th min
PA	0.29	0.03	0.03	0.03
Sphinc	0.10	0.07	0.04	0.04
1stCap	0.34	0.06	0.11	0.28
2ndCap	0.28	0.91	0.73	0.84
3rdCap	0.13	0.08	0.44	0.66

Fig. 2 |. Papaverine-induced vasodilation and L-NAME- and ET1-induced vasoconstrictions are attenuated in brain aging and are dependent on vascular mural cells.

a–c, Comparison of vessel dilation with 10 mM papaverine puffing. **a**,**b**, Representative images of vascular response to papaverine puffing in adult and old brains. Scale bar, 10 μm. Small insets show enlarged precapillary sphincters (scale bar, 10 μm). **c**, Comparison of relative dilation amplitude by papaverine puffing. Adult, $N = 8$ animals, $n = 17$ vessels; old, $N = 5$ animals, $n = 8$ vessels. **d**,**e**, Representative images of MIT in response to intravenous bolus infusion of L-NAME at a dose of 30 mg per kg body weight in adult (**d**) and old (**e**) mice. Scale bar, 20 μm. Small insets show enlarged precapillary sphincters (scale bar, 10 μm). **f**,**g**, Mean (solid curve) and s.e.m. (shadow) traces of the vessel diameter changes at each vascular location upon L-NAME infusion in adult and old mice. **h**, Comparison of relative diameter changes at 4th minute after L-NAME infusion. **i**, P values of statistical analysis for comparison of averaged constriction amplitudes at each vascular location at the 1st, 2nd, 3rd and 4th minutes after injection of L-NAME. Red highlighted grids show P values that are smaller than 0.05. Adult, $N = 5$ animals, $n = 5$ vessels; old, $N = 8$ animals, $n = 8$ vessels. Raw data for the intravenous infusion of L-NAME in adult brains were reused from our previous publication[11]. **j**,**k**, Representative images of MIT in response to 0.5 μM ET1 puffing in adult (**j**) and old (**k**) mice. Scale bar, 20 μm. Small insets show enlarged precapillary sphincters at the same imaging plane in the green channel. Scale bar, 10 μm. **l**,**m**, Mean (solid curve) and s.e.m. (shadow) traces of the vessel diameter change at each vascular location upon ET1 puffing. The initial diameter drop was due to a momentary mechanical pressure change caused by puffing. **n**, Comparison of relative dilation amplitude upon ET1 puffing. Adult, $N = 5$ animals, $n = 10$ vessels; old: $N = 7$ animals, $n = 15$ vessels. Raw data for ET1 puffing in adult brains were reused from our previous publication[11]. Linear mixed-effect models were used to test for differences among vessel segments, followed by Tukey post hoc tests for pairwise comparisons. Data are given as the mean ± s.e.m. $^{*}P < 0.05$, $^{**}P < 0.01$, $^{***}P < 0.001$. i.v., intravenous.

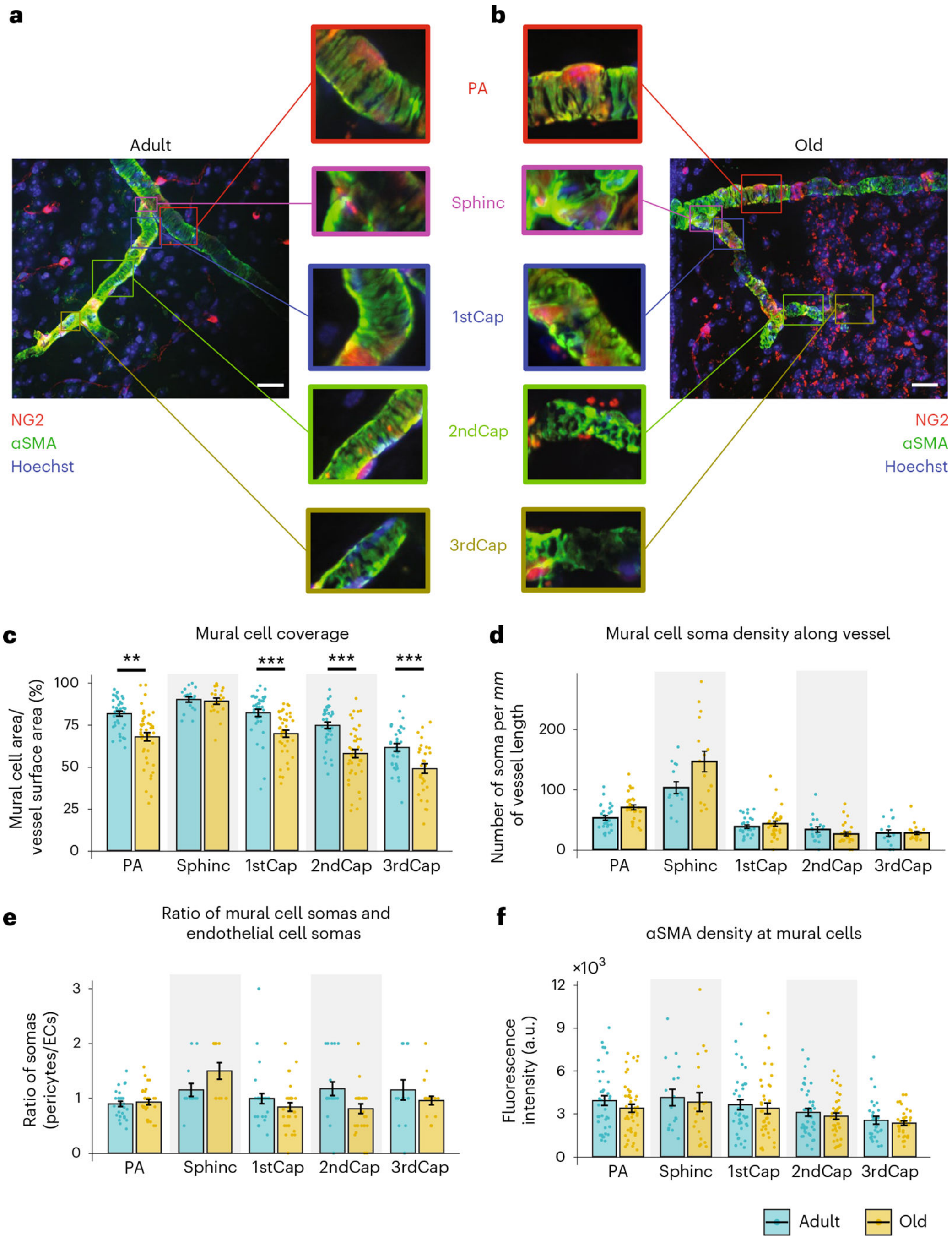

Fig. 3 |. Change of vascular mural cell structure at the microvascular inflow tract with age.

a,**b**, Maximum intensity projection of an adult (**a**) and old (**b**) brain image stack. Red, NG2; green, αSMA; blue, Hoechst. Enlarged insets of each vessel segment are presented in the middle for comparison. Scale bar, 10 μm. Note the vertical branch sprouting between first-order and second-order capillaries in **a**. Clearer individual planes are shown in Extended Data Fig. 9. **c**, Mural cell coverage of vessel surface obtained from dividing mural cell area by the total vessel surface area. **d**, Mural cell soma density along vessel calculated from the number of co-localized Hoechst and NG2 divided by vessel length. **e**, Mural cell soma number divided by endothelial cell soma number at each vessel location. **f**, αSMA density at mural cells obtained from calculating the mean αSMA fluorescence intensity at NG2-positive vessel areas. Adult, $N = 6$ animals, $n = 34$ vessels; old, $N = 6$ animals, $n = 40$ vessels. Linear mixed-effect models were used to test for differences among vessel segments, followed by Tukey post hoc tests for pairwise comparisons. Data are given as the mean ± s.e.m. *$P < 0.05$, **$P < 0.01$, ***$P < 0.001$. a.u., arbitrary units.

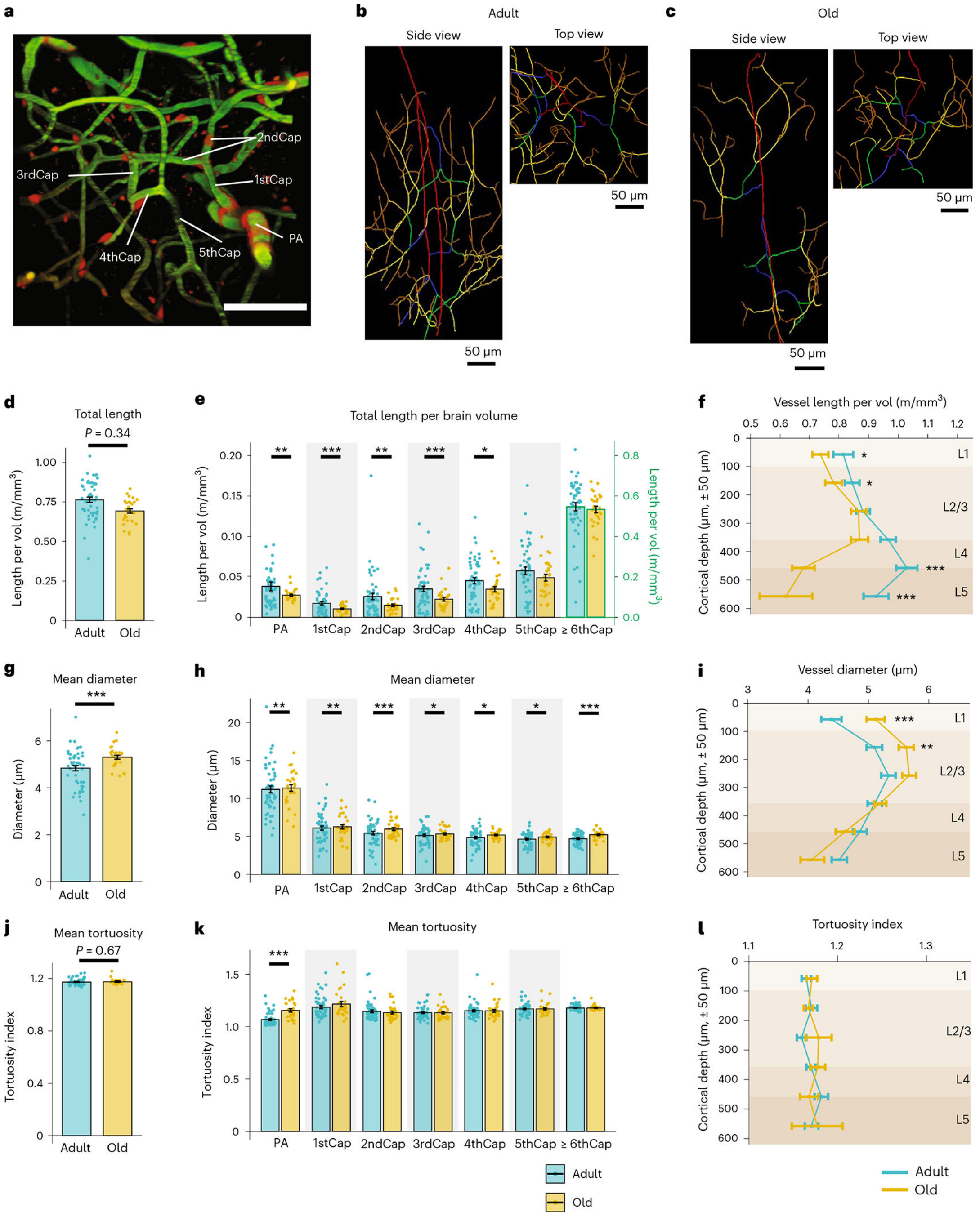

Fig. 4 |. Aging-induced angioarchitectural remodeling.

a, A representative image stack recorded by two-photon microscopy, containing the PA, the first-order capillary (1stCap), the second-order capillary (2ndCap), the third-order capillary (3rdCap), the fourth-order capillary (4thCap) and the fifth-order capillary (5thCap). Scale bar, 50 μm. **b**,**c**, Three-dimensional reconstructed vascular skeleton of the somatosensory cortex in an adult (**b**) and an old (**c**) mouse. Raw data were obtained by two-photon microscopy and analyzed by Amira software. Red, PAs; blue, 1stCap; green, 2ndCap; yellow, 3rdCap; orange, 4thCap; brown, 5thCap; purple, ascending venules. **d**–**f**, Vessel total length per brain volume in adult and old somatosensory cortex. General vessel total length (**d**), capillary-order-dependent vessel total length (**e**) and cortical depth-dependent vessel total length (**f**). **g–i**, Vessel mean diameter in adult and old somatosensory cortex. General mean diameter (**g**), capillary-order-dependent mean diameter (**h**) and cortical depth-dependent mean diameter (**i**). **j–l**, Vessel mean tortuosity in adult and old somatosensory cortex. The tortuosity index denotes division of the curved length by the chord length of each vessel segment. General mean tortuosity (**j**), capillary-order-dependent mean tortuosity (**k**) and cortical depth-dependent mean tortuosity (**l**). Adult, $N = 6$ animals, $n = 52$ vessels; old, $N = 6$ animals, $n = 29$ vessels. Linear mixed-effect models were used to test for differences among vessel segments, followed by Tukey post hoc tests for pairwise comparisons. Data are given as the mean ± s.e.m. $^{*}P < 0.05$, $^{**}P < 0.01$, $^{***}P < 0.001$. L1–L5 denote cortical sublayers.